Monthly Notices of the ROYAL ASTRONOMICAL SOCIETY

MNRAS **545,** 1–26 (2026) https://doi.org/10.1093/mnras/staf2064
Advance Access publication 2025 November 14

Unveiling the nature of the *Einstein Probe* transient EP241021a

J. Quirola-Vásquez [1]★ P. G. Jonker [1] A. J. Levan [1,2] D. B. Malesani [3,4] F. E. Bauer [5] N. Sarin [6] G. P. Lamb [7] A. Martin-Carrillo [8] J. Sánchez-Sierras [1] M. Fraser [8] L. Izzo [9,10] M. E. Ravasio [1] D. Mata Sánchez [11,12] M. A. P. Torres [11,12] J. N. D. van Dalen [1] A. P. C. van Hoof [1] J. A. Chacón [13,14] S. Littlefair [15] V. S. Dhillon [11,15] L. Cotter [8] G. Corcoran [8] R. A. J. Eyles-Ferris [16] P. T. O'Brien [16] D. Stern [17] F. Harrison [18] V. D'Elia [19] and D. H. Hartmann [20]

[1]*Department of Astrophysics/IMAPP, Radboud University Nijmegen, PO Box 9010, Nijmegen, NL-6500 GL, The Netherlands*
[2]*Department of Physics, University of Warwick, Coventry CV4 7AL, UK*
[3]*The Cosmic Dawn Centre (DAWN), Niels Bohr Institute, University of Copenhagen, Juliane Maries Vej 30, 2100, Copenhagen, Denmark*
[4]*Niels Bohr Institute, University of Copenhagen, Jagtvej 155, DK-2200, Copenhagen N, Denmark*
[5]*Instituto de Alta Investigación, Universidad de Tarapacá, Casilla 7D, Arica, 1010000, Chile*
[6]*The Oskar Klein Centre, Department of Physics, Stockholm University, AlbaNova, Stockholm, SE-106 91, Stockholm, Sweden*
[7]*Astrophysics Research Institute, Liverpool John Moores University, IC 2, Liverpool Science Park, 146 Brownlow Hill, Liverpool L3 5RF, UK*
[8]*School of Physics and Centre for Space Research, University College Dublin, Belfield, Dublin 4, Ireland*
[9]*Osservatorio Astronomico di Capodimonte, INAF, Salita Moiariello 16, Napoli, I-80131, Italy*
[10]*Niels Bohr Institute, University of Copenhagen, DARK, Jagtvej 128, Copenhagen, DK-2200, Denmark*
[11]*Instituto de Astrofísica de Canarias, E-38205, La Laguna, Tenerife, Spain*
[12]*Universidad de La Laguna, Departamento de Astroísica, E-38206, La Laguna, Tenerife, Spain*
[13]*Instituto de Astrofísica, Facultad de Física, Pontificia Universidad Católica de Chile, Campus San Joaquín, Av. Vicuña Mackenna 4860, Macul Santiago 7820436, Chile*
[14]*Millennium Institute of Astrophysics, Nuncio Monseñor Sótero Sanz 100, Of 104, Providencia, Santiago, Chile*
[15]*Astrophysics Research Cluster, School of Mathematical and Physical Sciences, University of Sheffield, Sheffield S3 7RH, UK*
[16]*School of Physics and Astronomy, University of Leicester, University Road, Leicester LE1 7RH, UK*
[17]*Jet Propulsion Laboratory, California Institute of Technology, 4800 Oak Grove Drive, Mail Stop 264-789, Pasadena, CA 91109, USA*
[18]*Department of Astronomy, California Institute of Technology, 1200 East California Blvd, Pasadena, CA 91125, USA*
[19]*Space Science Data Center (SSDC) – Agenzia Spaziale Italiana (ASI), Via del Politecnico snc, I-00133 Roma, Italy*
[20]*Department of Physics & Astronomy, Clemson University, Clemson, SC 29634, USA*

Accepted 2025 November 15. Received 2025 November 10; in original form 2025 July 19

ABSTRACT

We present a multiwavelength analysis of the fast X-ray transient EP241021a, discovered by the Wide-field X-ray Telescope aboard the *Einstein Probe* satellite on 2024 October 21. The event was not detected in gamma-rays. Follow-up observations from ∼1.5 to 100 d post-trigger were obtained across X-ray, ultraviolet, optical, near-infrared, and radio bands with ground- and space-based facilities. The redshift is constrained to $z = 0.7485$ from prominent optical spectral features. The optical light curve shows complex evolution: an initial $\sim t^{-0.7}$ decay, followed by a rapid re-brightening peaking at day 7.7 with $\sim t^{-1.7}$ decay, and a third phase peaking near day 19 with $\sim t^{-1.3}$ decay. The spectral energy distribution (SED) and its temporal evolution are consistent with a mix of non-thermal and thermal components. Early optical-to-X-ray spectral indices agree with optically thin synchrotron emission, while steepening of the optical SED after ∼20 d indicates either a shift in emission mechanism or the emergence of an additional component. Although broad-lined absorption features are absent, comparisons with Type Ic-BL supernovae suggest an SN contribution at late times, suggesting a collapsar origin for EP241021a. The likely SN in EP241021a appears to require an additional energy source beyond ^{56}Ni decay. These results support the view that some fast X-ray transients detected by the *Einstein Probe* arise from massive stellar explosions.

Key words: X-rays: bursts – gamma-ray bursts – transients: supernovae.

1 INTRODUCTION

Extragalactic fast X-ray transients (FXTs) are defined as bursts of soft X-ray photons (in the ∼0.3–10 keV band) with durations from seconds to hours (J. Heise & J. in't Zand 2010). Over the decades, our

★ E-mail: jonathan.quirolavasquez@ru.nl

knowledge of FXTs has increased substantially via the identification and characterization of sources detected by the new generation of X-ray satellites such as the Neil Gehrels *Swift* Observatory (*Swift*; e.g. A. M. Soderberg et al. 2008; P. A. Evans et al. 2023), the *Chandra* X-ray Observatory (e.g. P. G. Jonker et al. 2013; A. Glennie et al. 2015; J. A. Irwin et al. 2016; F. E. Bauer et al. 2017; Y. Q. Xue et al. 2019; D. Lin et al. 2022; J. Quirola-Vásquez et al. 2022, 2023), and the *X-ray Multi-mirror Mission–Newton telescope* (*XMM–Newton*; e.g. D. Alp & J. Larsson 2020; G. Novara et al. 2020; A. De Luca et al. 2021). The high spatial resolution of those X-ray Telescopes (XRTs) has mainly permitted ruling out any association with stellar flares, i.e. strengthening their extragalactic nature, as well as enabling the localization of the host galaxies of the transients (e.g. D. Eappachen et al. 2022; D. Lin et al. 2022; D. Eappachen et al. 2023, 2024; J. Quirola-Vásquez et al. 2025)¡.

Several different progenitor models have been suggested to explain the X-ray light curve and spectra of extragalactic FXTs, as well as the multiwavelength emission of contemporaneous counterparts: (i) the shock breakout (SBO) associated with certain types of core-collapse supernovae (CC-SNe) could produce an FXT, when the shock wave generated by a CC-SN reaches the surface of the progenitor star (e.g. SN2008D/XRF 080109; A. M. Soderberg et al. 2008; E. Waxman & B. Katz 2017; D. Alp & J. Larsson 2020; H. Sun et al. 2022; B. Scully, C. D. Matzner & A. Yalinewich 2023); (ii) some models involving binary neutron star (BNS) mergers lead to the formation of a millisecond spin period highly magnetized neutron star – a magnetar – that powers a nearly isotropic X-ray signal detectable as an FXT (e.g. XRT 141001, XRT 150322, and recently EP250207b; Z. G. Dai et al. 2006; B. D. Metzger, E. Quataert & T. A. Thompson 2008; Y.-W. Yu, B. Zhang & H. Gao 2013; B. Zhang 2013; H. Sun, B. Zhang & H. Gao 2017; H. Sun et al. 2019; J. Quirola-Vásquez et al. 2024b; P. G. Jonker et al. 2026); (iii) recently, some FXTs have shown a connection with luminous fast blue optical transients (LFBOTs), and/or broad-lined Type Ic SNe (e.g. EP240414a and EP250108a; H. Sun et al. 2025; J. N. D. Dalen et al. 2025; R. A. J. Eyles-Ferris et al. 2025; W. X. Li et al. 2025; J. C. Rastinejad et al. 2025; G. P. Srinivasaragavan et al. 2025; S. Srivastav et al. 2025); (iv) a subset of FXTs may originate from the tidal disruption of a white dwarf (WD) passing close to an intermediate-mass black hole (IMBH, $\sim 10^3$–10^5 $M_\odot$; e.g. XRT 000519 and EP240408a; P. G. Jonker et al. 2013; M. MacLeod et al. 2016; K. Maguire et al. 2020; B. O'Connor et al. 2025); and (v) high-redshift and low-luminous gamma-ray bursts (GRB) would naturally be redshifted to the X-ray range by cosmic expansion (e.g. EP240315a and EP240801a; J. H. Gillanders et al. 2024; A. J. Levan et al. 2025; S.-Q. Jiang et al. 2025; W. X. Li et al. 2025). Nevertheless, until 2024, in the vast majority of cases, the X-ray transients themselves have only been identified long after the X-ray trigger, rendering contemporaneous follow-up observations impossible. Hence, determining their energetics and distance scale, and, by extension, their physical origin, remained a challenge.

The *Einstein Probe* (EP; W. Yuan et al. 2015, 2022, 2025) satellite, launched on 2024 January 9, is enabling a transformation of the field, discovering ≈120 new extragalactic FXTs in the first ∼1.5 yr of operations. EP contains the Wide-field X-ray Telescope (EP-WXT) with a field of view (FoV) of 3600 sq deg, the first wide-field imaging survey instrument operating in the soft X-ray band (0.5–4 keV). It is specifically designed for precise localization and rapid reporting of FXTs. The delay between discovery and multiwavelength follow-up observations is reduced even by up to a factor of $\sim 10^4$ in time with respect to the FXTs discovered by *Chandra* or *XMM–Newton*. In addition, in several cases, the Follow-up X-ray Telescope onboard EP (EP-FXT) subsequently provides an accurate X-ray position to a few tens of arcseconds on time-scales of order an hour or even less when the EP-WXT triggers an onboard automatic slew to the EP-FXT instrument, and for a subsample of these optical/near-infrared (NIR) counterparts have been identified.

Recently, the FXT EP240414a was discovered by the EP satellite (H. Sun et al. 2025; J. S. Bright et al. 2025; J. N. D. Dalen et al. 2025; S. Srivastav et al. 2025). It was found at a redshift of $z \approx 0.4$ and associated with a massive host galaxy, located at a large projected physical offset of ≈26 kpc (J. N. D. Dalen et al. 2025; S. Srivastav et al. 2025). According to the Amati relation, its energetics are consistent with those of low-luminosity GRBs (H. Sun et al. 2025). The optical light curve showed an initially slow decline (inconsistent with afterglow emission; J. N. D. Dalen et al. 2025), followed by a re-brightening to $M_r \approx -21$ mag at day ∼2 in rest frame (rising from the interaction with the stellar envelope and a dense circumstellar medium, CSM), consistent with the behaviour of LFBOTs. Furthermore, at later epochs (after ∼15 d, rest frame), a third component emerged, peaking at $M_r \approx -19.5$ mag, coinciding with the spectroscopic confirmation of a Type Ic-BL SN. This spectroscopic identification confirms a massive star as the progenitor of the transient, making EP240414a the first object to establish a direct link between the progenitors of long-duration GRBs, FXTs, and (potentially) LFBOTs (J. N. D. Dalen et al. 2025). Although other scenarios can also be possible (e.g. J.-H. Zheng et al. 2025).

In this paper, we study in detail the EP transient EP241021a. EP241021a is a newly discovered FXT detected on 2024 October 21 by the EP satellite through its EP-WXT instrument (J. W. Hu et al. 2024). The transient exhibited a luminous soft X-ray flash with a duration of approximately ∼100 s and a peak 0.5–4 keV luminosity of $\sim 10^{48}$ erg s^{-1} (X. Shu et al. 2025) at a redshift of $z \approx 0.75$ (G. Pugliese et al. 2024). No gamma-ray counterpart was detected for this event (E. Burns et al. 2024). Recently, this transient has been studied in detail by different groups using radio, optical, NIR, and X-ray data (e.g. M. Busmann et al. 2025; G. Gianfagna et al. 2025; X. Shu et al. 2025; G.-L. Wu et al. 2025; M. Yadav et al. 2025),which suggested different interpretations. The optical and NIR light curves show an initially slow decay followed by a steeper rise after a few days, peaking at an absolute magnitude of $M_r \approx -22$ mag (M. Busmann et al. 2025). The multiwavelength spectral energy distribution (SED, until day ∼ 18 after the detection) is consistent with a non-thermal origin ($r - J \approx 1$ and $r - z \approx 0.4$; M. Busmann et al. 2025; X. Shu et al. 2025). Some authors suggest an association with a mildly relativistic outflow from a low-luminosity GRB (M. Busmann et al. 2025), or the interaction of a complex/multicomponent jet (from a highly relativistic narrow cone to much a broader and mildly relativistic cocoon) with the environment of the pre-existing progenitor (G. Gianfagna et al. 2025; M. Yadav et al. 2025). Alternative scenarios considered include a catastrophic collapse/merger of a compact star system leading to the formation of a millisecond magnetar (G.-L. Wu et al. 2025) or a jetted tidal disruption event (TDE) involving three jet ejections (X. Shu et al. 2025).

Here, we report on the multiwavelength data set of the FXT EP241021a (J. W. Hu et al. 2024) that our team gathered. We present extensive imaging and spectroscopic observations spanning from ∼1.5 to 300 d after the EP-WXT trigger. We analyse our data set in combination with the data reported in the literature (M. Busmann et al. 2025; G. Gianfagna et al. 2025; X. Shu et al. 2025; G.-L. Wu et al. 2025; M. Yadav et al. 2025). In Section 2, we introduce the multiwavelength observations used in this work. In Section 3, we describe the most significant results obtained by analysing the multiwavelength data. Section 4 shows a phenomenological discussion on the nature of EP241021a, event rate density of similar

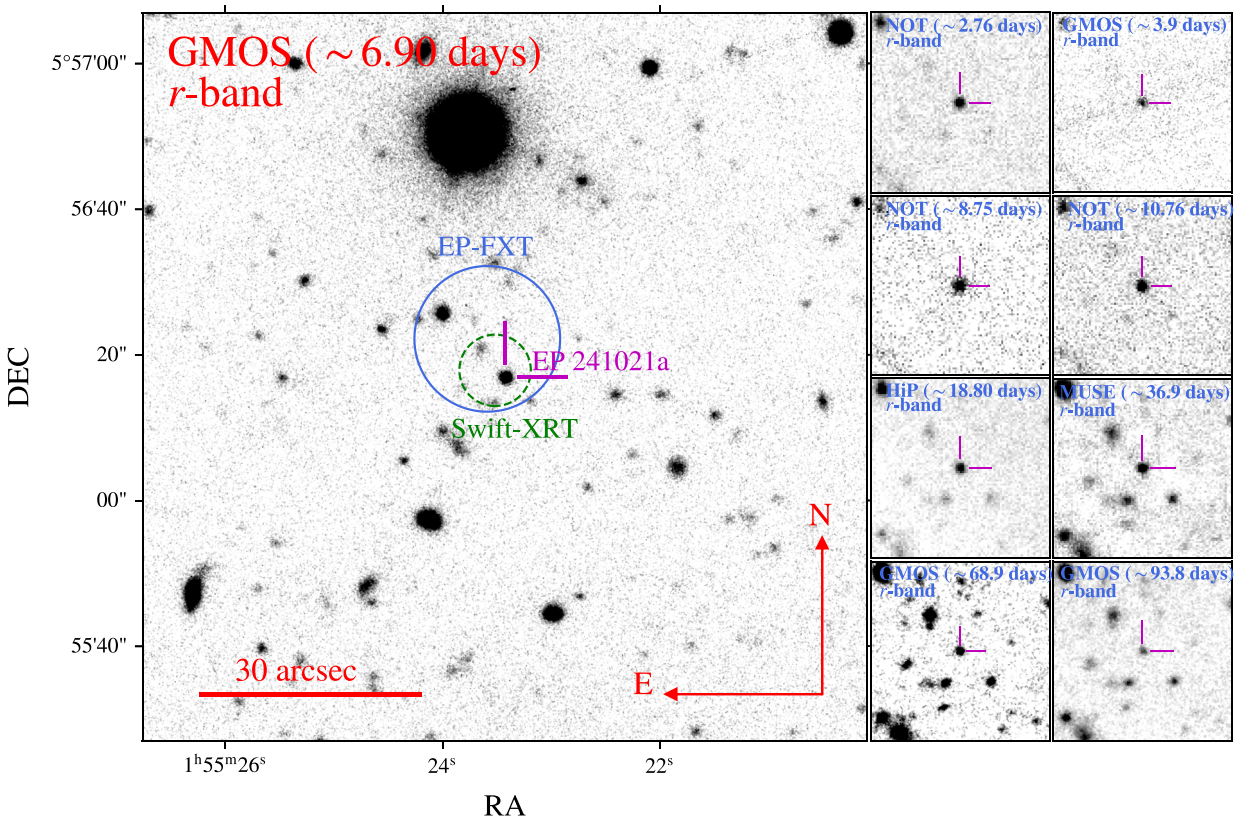

Figure 1. *r*-band image of the X-ray transient EP241021a; the position of the event is marked by lines. The large panel is made from the GMOS observation of EP241021a at day ∼ 6.9. The solid (10 arcsec radius) and dashed (4.9 arcsec radius) circles show the location of the transient reported by the EP-FXT and *Swift*-XRT, respectively. The lateral panels display eight snapshots of the photometric evolution in *r* band of the transient, from day ∼ 2.76 to 93.8, taken by different telescopes.

transients (Section 4.7), and host galaxy properties (Section 4.6). Meanwhile, our multiwavelength light-curve modelling is presented in Section 5. Finally, in Section 6, we summarize our main results and interpretation. Throughout we provide magnitudes in the AB system, and for NIR magnitudes calibrated to the Two Micron All Sky Survey (2MASS), which is in the Vega system, we use the Vega to AB conversions $J_{\rm AB} = J_{\rm VEGA} + 0.91$, $H_{\rm AB} = H_{\rm VEGA} + 1.39$, and $K_{s,\rm AB} = K_{s,\rm VEGA} + 1.85$ (M. R. Blanton & S. Roweis 2007). We assume a Lambda-cold dark matter cosmology with $H_0 = 67.66$ km s^{-1} Mpc^{-1} and $\Omega_\Lambda = 0.69$.

2 OBSERVATIONS

The EP-WXT detected the X-ray transient EP241021a on 2024-10-21 05:07:56 UTC (J. W. Hu et al. 2024). The source had a peak flux of $\sim 1 \times 10^{-9}$ erg s^{-1} cm^{-2} in the 0.5–4 keV band, while its average spectrum can be fitted with an absorbed power law with a photon index of $\Gamma = 1.5 \pm 1.2$ and a fixed Galactic column density of $N_{\rm H,Gal} = 5 \times 10^{20}$ cm^{-2}, at an average unabsorbed 0.5–4 keV flux of $3.3^{+4.8}_{-1.6} \times 10^{-10}$ erg s^{-1} cm^{-2} at a 90 per cent confidence level (J. W. Hu et al. 2024).

Observations taken by the Nordic Optical Telescope (NOT; T. Andersen et al. 1992), starting at ∼1.77 d after the X-ray trigger, revealed an uncatalogued optical source within the EP-WXT uncertainty position, at coordinates RA$_{\rm J2000.0} = 01^{\rm h}55^{\rm m}23^{\rm s}.41$, Dec.$_{\rm J2000.0} = +\,05^\circ56'18''.01$ (with uncertainty of 0.5 arcsec; although no confidence interval was given by S. Y. Fu et al. 2024a), with a magnitude of $m_z = 21.6 \pm 0.11$ and $m_r = 21.95 \pm 0.06$ mag (S. Y. Fu et al. 2024a). Because of the temporal and spatial coincidence, this source was suggested to be the optical counterpart of EP241021a. This was confirmed through multiple independent optical observations taken by the Thai Robotic Telescope network located at Fresno, California, US (TRT-SRO), the 0.76-m Katzman Automatic Imaging Telescope (KAIT) located at Lick Observatory, and the Liverpool Telescope (LT) located at the Observatorio del Roque de los Muchachos, La Palma, Spain (A. K. Ror et al. 2024; S. Y. Fu et al. 2024b; W. X. Li et al. 2024b, b) who reported variability in the optical brightness. The counterpart was further confirmed by an X-ray observation taken by the EP-FXT (∼36.5 h after the EP-WXT detection), which refined the X-ray position to be consistent with the proposed optical counterpart (Y. Wang et al. 2024).

Our optical spectroscopic observations began using the FOcal Reducer and low dispersion Spectrograph (FORS; I. Appenzeller et al. 1998) mounted on the Very Large Telescope (VLT) ∼3 d after the EP-WXT trigger. The identification of a strong emission line [O II] at 6519 Å and the doublet absorption Mg II at 4897 Å, suggests a counterpart redshift of $z \approx 0.75$ (G. Pugliese et al. 2024). Subsequent independent spectroscopic observations using the Gran Telescopio Canarias (GTC, I. Pérez-Fournon et al. 2024), Keck (W. Zheng et al. 2024b), and GS (this work) telescopes confirm the redshift of the transient.

Several ground- and space-based telescopes observed the transient EP241021a over the period ranging from ∼1.7 to 100 d after the X-ray trigger. Fig. 1 shows the environment as well as eight imaging

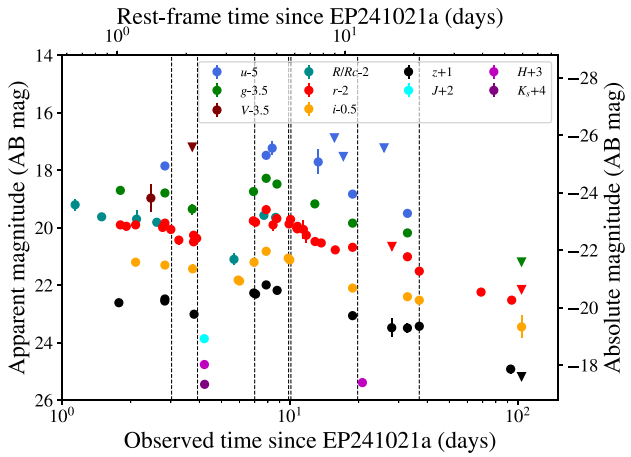

Figure 2. Apparent (left *Y*-axis) and absolute (right *Y*-axis) magnitude light curves of FXT EP241021a in the observer- (bottom *X*-axis), and rest frame (top *X*-axis) in several optical and NIR bands. The times at which our spectroscopic observations were taken are marked by the vertical dashed lines.

snapshots highlighting the photometric evolution of the transient EP241021a in the r band from day $\sim$ 3.76 to 93.8. From Sections 2.1 to 2.8, we introduce the multiwavelength observations used in this work (chronologically sorted), as well as a description of the data reduction methods. The optical and NIR photometric light curves of EP241021a are shown in Fig. 2, while the optical spectra of the transient are in Fig. 3. All the photometry is aperture photometry and calibrated to the Panoramic Survey Telescope & Rapid Response System (Pan-STARRS), Legacy, or 2MASS stars in the field.

The photometric results, derived in this work, are provided in Table A1. Moreover, throughout this manuscript, we used multiwavelength data taken from the General Coordinates Network (GCN) and the literature (see Tables A2–A4, including references to the original works).

2.1 Nordic Optical Telescope: ALFOSC camera

We also observed the target using the Andalucia Faint Object Spectrograph and Camera (ALFOSC) mounted on the NOT at the Roque de los Muchachos observatory (Canary Islands, Spain) on multiple epochs (from $\sim$1.7 to 15.8 d after the trigger) in the g, r, and z bands (program NOT 70–301, PI: Jonker). We use a standard dithering pattern for all observations, while the images were reduced with standard reduction steps employing IRAF (D. Tody 1986).

2.2 Gran Telescopio Canarias

The GTC at the Roque de los Muchachos observatory (Canary Islands, Spain) observed the source using the OSIRIS+ (Optical System for Imaging and low-intermediate-Resolution Integrated Spectroscopy), HiPERCAM (High PERformance CAMera), and EMIR (Espectrógrafo Multiobjeto Infra-Rojo) instruments on several nights (program GTC1-24ITP, PI: Jonker).

2.2.1 *OSIRIS + spectroscopy*

We obtained two spectroscopic epochs of the optical counterpart of EP241021a with the upgraded OSIRIS + instrument (J. Cepa et al. 2000). The first spectrum of the target was obtained on 31 October (i.e. $\sim$9.9 d, after the X-ray trigger) using an exposure time of 3×1800 s, the grism $R500R$ (covering $\approx$5000–9000 Å), and a 1 arcsec slit width placed at a position angle North–South. The second epoch was taken on November 9 (i.e. 19.8 d after the X-ray trigger) using an exposure time of 3×1800 s, the grism $R300B$ (covering $\approx$4000–8500 Å), and a 1 arcsecslit width placed aligned East–West. The data of both spectroscopic epochs were reduced in the same way: the data were corrected for bias and flat-field, and the source spectrum was extracted using standard `PyRAF` tasks. Cosmic rays were removed using `LACosmic` (P. G. Dokkum 2001). The wavelength calibration was done using daytime arc-lamp observations using MOLLY. The flux calibration was done through observations of a standard star taken on the same night.

2.2.2 *HiPERCAM photometry*

We obtained photometric data of our target using the HiPERCAM (V. S. Dhillon et al. 2021) in the $ugriz$ bands, simultaneously, during five different epochs of 40×30 s exposure time: 2025 October 24 (i.e. $\sim$ 2.8 d after the trigger), October 29 (i.e. $\sim$ 7.9 d after the trigger), November 9 (i.e. $\sim$ 18.8 d after the trigger), November 22 (i.e. $\sim$ 32.7 d after the trigger), and February 1 (i.e. $\sim$ 103.7 d after the trigger). The obtained data were reduced with the HiPERCAM pipeline (V. S. Dhillon et al. 2021). The source is detected in all bands. Moreover, to detect the host galaxy of the transient, we observed the transient's sky location using HiPERCAM on 2025-08-21 03:38:10.9 UTC (i.e. $\sim$304 d after the X-ray trigger), when the light of the transient had disappeared, obtaining photometry of the host in the $ugriz$ bands simultaneously, using 120×30 s exposures. The results of the host galaxy detection and photometry are available in Section 4.6.

2.2.3 *EMIR photometry*

The target was also observed by the EMIR (F. Garzón et al. 2022) in the NIR range on November 10 (i.e. $\sim$20.8 d after the X-ray trigger). The target was observed in the H band for 1280 s, where the target was detected. The EMIR data were reduced using PYEMIR (S. Pascual et al. 2010; N. Cardiel et al. 2019) and standard IRAF tasks (D. Tody 1986) to perform flat-field correction and stack individual frames.

2.3 Very Large Telescope

2.3.1 *FORS2 spectroscopy*

The FORS2 instrument (I. Appenzeller et al. 1998) was used to obtain spectroscopy (program ESO 114.27PZ, PI: Tanvir) using the $300V$ grism (covering $\approx$3300–6600 Å), an exposure time of 4×1200 s, and a 1 arcsec slit width on 24 October ($\sim$3 d after the trigger). We reduced the spectroscopic observations using the FORS2 `esoreflex` pipeline (W. Freudling et al. 2013; ESO CPL Development Team 2015). We flux-calibrated the spectrum employing observations of the spectrophotometric standard obtained with the same setup.

2.3.2 *Multi Unit Spectroscopic Explorer*

We obtained an observation of EP241021a with the MUSE (Multi Unit Spectroscopic Explorer) instrument (covering $\approx$4800–9300 Å; R. Bacon et al. 2010) on November 27, i.e. $\sim$37 d since the trigger (program ESO 111.259Q, PI: Jonker), and an exposure time of 4×700 sec. The data was reduced using the MUSE `esoreflex` pipeline (ESO CPL Development Team 2015; P. M. Weilbacher et al. 2020), and additional sky subtraction was performed with the Zurich Atmosphere Purge (ZAP) package (K. T. Soto et al. 2016).

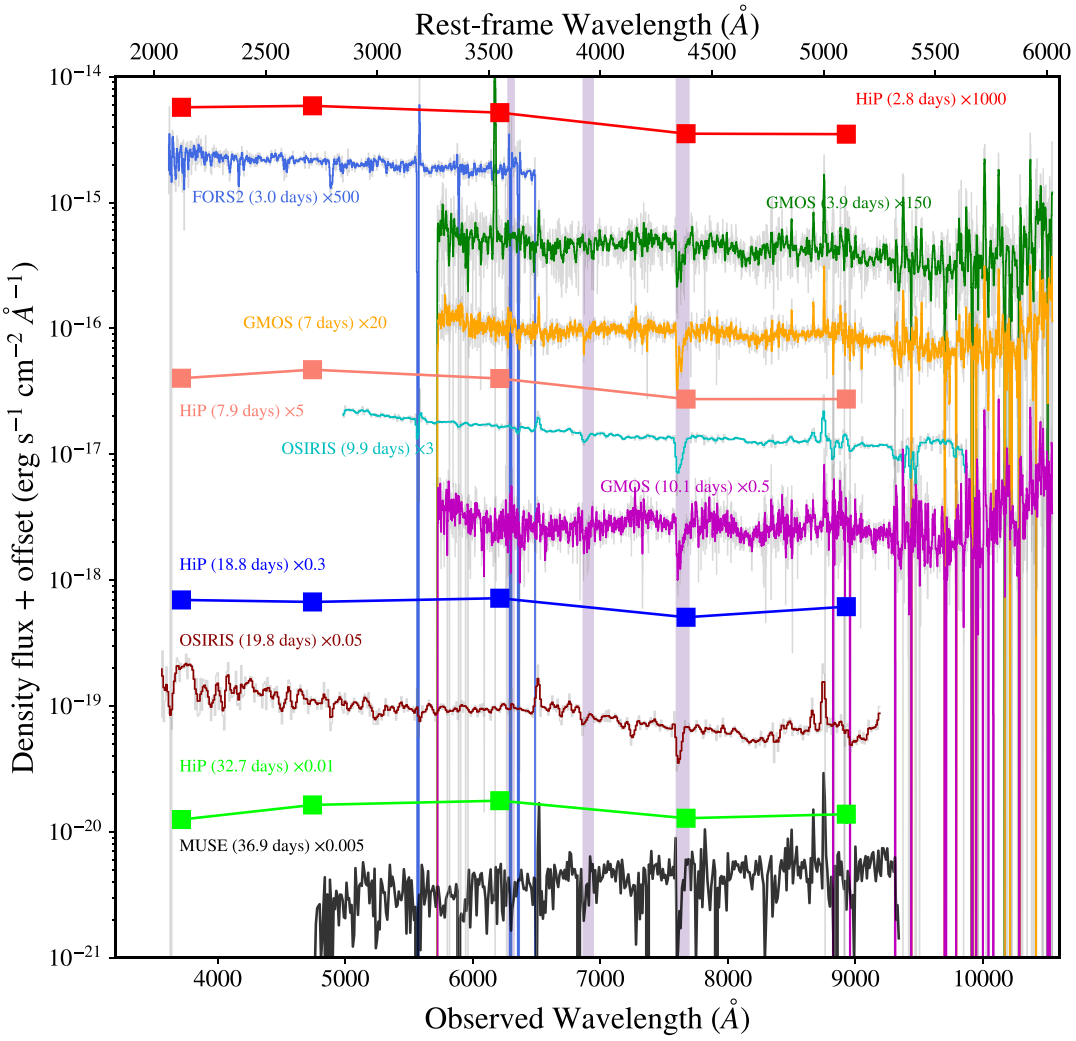

Figure 3. Evolution of the optical spectra of the counterpart of FXT EP241021a in the observer (bottom *X*-axis) and rest (top *X*-axis) frame. The spectrum obtained first is shown at the top, and the last one is at the bottom (the times in brackets next to the spectra indicate the days after the WXT trigger, in the observer frame). In addition, we also show the flux density measured using our four GTC/HiPERCAM observations (*ugriz* bands). Vertical regions corresponding to telluric absorption are shaded.

The reduced MUSE cube was visually inspected using the viewer package `QFitsView` (T. Ott 2012). We created broad-band images in the r, i, and z bands using the PYTHON package PYMUSE (I. Pessa, N. Tejos & C. Moya 2018). For the spectral extraction, we also use PYMUSE, and a circular aperture of 8 pixels (i.e. 1.6 arcsec aperture) because of the point-like nature of the target. For combining pixels within the spectral extraction aperture, we use the mode 'White Weighted Mean'. In this mode, the spectrum from an aperture is a weighted sum of the spaxels by a brightness profile obtained from the white-light image.

2.4 Gemini-South: The Gemini Multi-Object Spectrographs

The target was observed using the GMOS (Gemini Multi-Object Spectrographs) instrument (I. M. Hook et al. 2004; G. Gimeno et al. 2016), mounted on the Gemini-South (GS) telescope at Cerro Pachón, Chile. GMOS was operated in imaging mode during several epochs between ∼7 to 95 d after the X-ray trigger (using programs GS-2024B-Q-131 and GS-2024B-FT-112, Bauer PI). We reduced GMOS imaging data using the DRAGONS pipeline (K. Labrie et al. 2023a, b) and followed standard recipes for the imaging and spectroscopic observations. In addition to the photometric data, we obtained a spectrum of the optical counterpart of EP241021a at three different epochs, namely, on October 25 at ∼3.9 d, on October 28 at ∼7 d, and on October 31 at ∼10.1 d, with a total on-target exposure time of 4 × 900, 4 × 1500, and 4 × 1200 s, respectively. Our spectroscopic observations were all carried out using the GMOS-S instrument (program GS-2024B-Q-131, Bauer PI), the *R*400 grating, a 1 arcsec slit width, and with the slit oriented at the parallactic angle. The spectra cover the wavelength range ≈4200–9100 Å. Moreover, the reduced spectra were flux calibrated using a standard star taken on previous nights of the spectroscopic observations. During the three spectroscopic epochs, there are a number of emission lines evident in the spectrum that can be used to estimate the redshift of the system.

2.5 Keck Telescope: MOSFIRE

NIR imaging observations, using the Multi-Object Spectrograph for Infrared Exploration (MOSFIRE; I. S. McLean et al. 2012) at the Keck I telescope (Mauna Kea, Hawaii) were taken using the

broad-band filters J, H, and K_s on October 25 (i.e. ∼4.2 d after the X-ray trigger), with exposures of 5×60, 6×30, and 9×60 s, respectively. The data were reduced with the software package THELI version 3.1.3 (T. Erben et al. 2005; M. Schirmer 2013). Clear detections of the counterpart were obtained in the three NIR bands.

2.6 Southern Astrophysical Research Telescope: the Goodman Red and Blue Camera

The Goodman Blue and Red Camera instruments mounted on the 4.1-m SOAR (Southern Astrophysical Research) Telescope located on Cerro Pachón, Chile (J. C. Clemens, J. A. Crain & R. Anderson 2004) were used to observe the optical counterpart of EP241021a, during four different epochs (program SOAR2024B-016, PI: Bauer). Data were obtained on October 27 at ∼5.9 d after the EP-WXT trigger (using i band), on October 31 at ∼9.9 d since the trigger (using r and i bands), on November 3 at ∼12.8 d since the trigger (using g and r bands), and on November 18 at ∼27.9 d after the trigger (using r and z bands). The data were bias-subtracted and flat-field corrected adopting standard `PyRAF`tasks (Science Software Branch at STScI 2012), and cosmic rays were removed using the `LACosmic` task (P. G. Dokkum 2001). The world coordinate system information is implemented using `astrometry.net` codes (D. Lang et al. 2010). The counterpart of EP241021a was clearly detected during the first three epochs and marginally detected during the last one.

2.7 Neil Gehrels *Swift* Observatory

The *Swift* satellite (N. Gehrels et al. 2004) observed the location of EP241021a on seven different epochs, with the XRT and the UltraViolet/Optical Telescope (UVOT). The data span the time range between ∼4.5 and 25.9 d after the trigger, for a total exposure time of about ∼17.3 ks.

2.7.1 *X-ray Telescope*

From the data products generator online tool provided by the University of Leicester (P. A. Evans et al. 2007, 2009),[1] the X-ray afterglow of EP241021a was detected, localized at $\mathrm{RA_{J2000}} = 01^{\mathrm{h}}55^{\mathrm{m}}23^{\mathrm{s}}.52$, $\mathrm{Dec._{J2000}} = +\ 05^{\circ}56'17''.8$ with uncertainty of 4.9 arcsec at 90 per cent confidence level (using HEASOFT v6.35.2). We extracted the source count rate using the command line interface XSELECT (J. Ingham & K. Arnaud 2006) and HEASOFT v6.32, using a region of 40 arcsec radius centred at the position of the optical counterpart (S. Y. Fu et al. 2024a), while the background counts were extracted from a larger region (60 arcsec) near the source. The corresponding response files for spectral fits were created with the latest calibration available for *Swift* data (updated version 2024 May). Unfortunately, a detailed spectral analysis per individual observation is not possible due to the low number of X-ray counts. Moderate detections (i.e. S/N$\gtrsim$3) were achieved only at two epochs (∼8.3 and 25.8 d after the trigger). Our results are consistent with the count-rate light curve retrieved by the data products generator tool. Combining and fitted all epochs using a power-law model (and a fixed Galactic hydrogen column density of 5×10^{20} cm^{-2}; P. M. W. Kalberla et al. 2005; R. Willingale et al. 2013; P. M. W. Kalberla & U. Haud 2015) yields a photon index of $\Gamma = 2.3^{+1.3}_{-0.7}$ and an unabsorbed energy conversion factor of 3.1×10^{-11} erg cm^{-2} count^{-1} (used to transform the count rate to flux units). Table A3 shows the derived unabsorbed fluxes of the target.

[1] https://www.swift.ac.uk/user_objects/

2.7.2 *UltraViolet/Optical Telescope*

Furthermore, we analysed the images obtained by the *Swift*–UVOT in the optical and UV filters. *Swift*–UVOT observed the target with filters V, U, and $UVM2$ during seven different epochs. The filters V and $UVM2$ were used only during two epochs (∼3.7 and 4.5 d) and U band during the other observations. To measure photometry, we used the script `uvotsource`, which performs aperture photometry on a single source in a UVOT sky image. We use a circular aperture of 4 arcsec (because of the faintness of the target). The package is part of the HEASOFT software package (J. K. Blackburn 1995). During days ∼8.3 and 13.3, the target was significantly (S/N≈5) and marginally (S/N≈3) detected, respectively, using filter u.

2.8 *Chandra* X-ray Observatory

The *C handra* satellite observed the location of EP241021a on November 4 (∼14 d after the trigger) for a total exposure time of 10 ks (Director's Discretionary Time; PI: Jonker). The source position was placed at the S3 CCD of the Advanced CCD Imaging Spectrometer (ACIS-S) detector array using the very faint mode for read-out (G. P. Garmire 1997). We analyse the data using the package CIAO version 4.16 (Chandra Interactive Analysis of Observations; A. Fruscione et al. 2006), reprocessing the events using the task ACIS_REPROCESS_EVENTS, taking the VERY FAINT data telemetry mode into account. Using WAVDETECT (P. E. Freeman et al. 2002) to detect sources, we detect X-ray emission spatially coincident with the location of the optical counterpart of EP241021a. The spectrum was extracted via the CIAO package `specextract`. To obtain the X-ray spectral parameters, we used the spectral-fitting program XSPEC v12.14 (K. A. Arnaud 1996) and considered the Cash statistic (W. Cash 1979) to account for the low number of counts of the target (26 counts inside an circular aperture region with a radius of 1.5 arcsec). We fit an absorbed power-law model (`tbabs*pow` model in XSPEC) to the spectrum binned to have at least one photon per bin, where the `tbabs` model describes the Galactic absorption. For the extraction of the X-ray spectral parameters, we fixed the Galactic hydrogen column density to 5×10^{20} cm^{-2} (P. M. W. Kalberla et al. 2005; P. M. W. Kalberla & U. Haud 2015). The absorbed fluxes are computed using the standard XSPEC tasks, while the unabsorbed fluxes are computed by the XSPEC convolution model `cflux` (see Table A3). The best-fitting power-law index is $\Gamma = 1.3\pm0.7$ (at 90 per cent confidence level) and the best-fitting source absorbed flux $F_X = \left(6.5^{+3.1}_{-2.0}\right)\times10^{-14}$ erg cm^{-2} s^{-1} at 0.3–10 keV for a C-stat of 21.76 for 21 degrees of freedom (d.o.f.).

3 RESULTS

3.1 Redshift and energetics

The redshift of $z = 0.75$ was determined from emission lines in the 2D spectra of the target by multiple groups with different instruments (I. Pérez-Fournon et al. 2024; G. Pugliese et al. 2024; W. Zheng et al. 2024b). To refine the reported redshift, we fitted the emission lines with the highest S/N (Hβ, [O II] λ3727, [O III]λλ4959,5007) using multiple Gaussian functions, to the GMOS and OSIRIS + spectroscopic epochs, and obtained the best-fitting central wavelengths

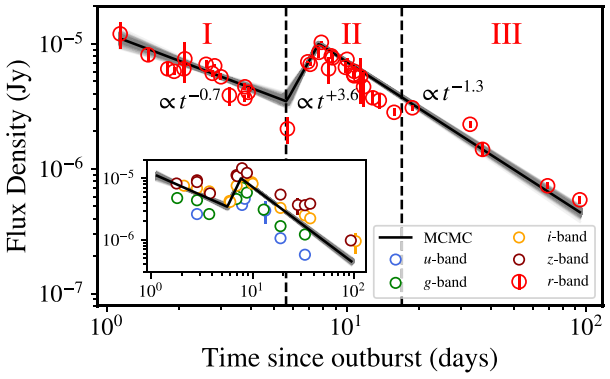

Figure 4. r-band light-curve fit of the FXT EP241021a using a smooth triple-power-law model (black line). The source flux decays initially following approximately a power law, then it re-brightens around $t_1 = 5.6 \pm 0.2$ d reaching a peak flux at $t_2 = 7.7 \pm 0.1$ d, and it subsequently decays, which can be described approximately by another power law. The Roman numbers at the top depict the three epochs of the light curve: (I) initial decay at $t \lesssim 6$ d; (II) re-brightening and a peak emission followed by a decay at $6 \lesssim t \lesssim 18$ d; and (III) a re-brightening followed by power-law decay starting at $t \approx 18$ d. We can expect a similar light-curve behaviour in other bands; however, the sampling cadence is not identical for all of them. Moreover, the inside figure depicts a comparison between the smooth triple-power-law model and $ugiz$ data. The units in the inside plot are the same as the large plot.

and their associated errors. Table A6 shows the derived redshift per spectroscopic epoch, with a mean value of $\overline{z}_{\rm spec} = 0.7485$. Moreover, we detect absorption lines of the Mg II doublet λλ2796, 2803 in the FORS2 spectrum at centroid wavelengths consistent with the redshift derived from the emission line fits. We interpret the emission lines as due to ionized gas in the host galaxy. At this redshift, the transient has a peak luminosity of $L_{\rm X,peak} \approx 2 \times 10^{48}$ erg s^{-1} in the 0.5–4 keV energy band.

3.2 Optical light curve

The optical and NIR light curves are shown in Fig. 2. The earliest observation of the target (using the KAIT) yields an apparent magnitude of $m_R = 21.2 \pm 0.2$ mag (W. Zheng et al. 2024a), i.e. an absolute magnitude of $M_R \sim -21.6$ mag at ∼1.14 d after the EP-WXT detection. We decided to add this photometric point (and others from literature, see Table A2) to the r-band light curve[2] Looking at the optical light curves, we can identify different trends during its evolution.[3] Fig. 4 depicts the fitting of the r-band light curve, which is the best sampled out of the light curves, considering a smooth triple-power-law model. In addition, in the inset in Fig. 4, we show the comparison between the best-fitting model to the r-band light curve and the $ugiz$ light curves to inspect how the multiwavelength light curve behaves with respect to that of the r band; it is clear that the transient becomes redder with time. Overall, the optical light curve shows two peaks: the first around ∼1 d (no observations prior to this epoch have been reported), and a second one at 7.7 ± 0.1 d (see Fig. 4). During the first ∼6 d, the light curves in all the optical bands decrease as a power-law function, with a power-law index of $\alpha_1 = -0.7 \pm 0.1$, i.e, $\Delta m \approx 1.9$ mag over this period.

After $t \approx 5.6$ d, the source re-brightened in all the bands (reported by J. A. Quirola-Vasquez et al. 2024a), with a steep slope of $\alpha_2 = +3.6 \pm 0.6$. The absolute magnitude reached a peak at 7.7 ± 0.1 d of $M_g \approx -21.0$, $M_r \approx -21.4$, $M_i \approx -21.5$, and $M_z \approx -21.8$ mag ($\Delta m_{griz} \approx 1.0 - 1.7$ mag).

Subsequently, the light curves decrease rapidly. Fitting all data beyond ≈ 7.7 d, we obtain a power-law index of $\alpha_3 = -1.3 \pm 0.1$ (see Fig. 4). Considering only data from ≈ 7.7 to 16 d, a power-law decay in the $griz$ bands ($\alpha_g = -1.7 \pm 0.1$, $\alpha_r = -1.7 \pm 0.2$, $\alpha_i = -1.4 \pm 0.1$, and $\alpha_z = -1.1 \pm 0.1$) describes the data well, where the decline from the peak is $\Delta m_{griz} \approx$1.0–1.6 mag over about 8.3 d.

In the case of the r-band light curve, a mild re-brightening occurred at day ∼18, reaching an absolute peak of $M_r \approx -20.1$ mag at day ∼19. This behaviour is not visible in the other bands, probably because of the lower cadence of our observations in those other bands. However, it also appears in observations of other groups (e.g. M. Busmann et al. 2025). The r-band light curve declines again after day ∼19. The behaviour in the z band is different; here the flux remains constant around days ∼ 27 and 37, followed by a decay.

The evolution of the light curve led us to categorize it into three epochs depicted in Fig. 4 by roman numbers: (I) initial decay until $t \lesssim 6$ d; (II) re-brightening and second decay between $6 \lesssim t \lesssim 18$ d; and (III) re-brightening followed by a final decay beyond $t \gtrsim 18$ d. There are no short-time optical flares of the transient in the multiple HiPERCAM epochs[4] (using the pipeline developed by V. S. Dhillon et al. 2021).

To explore the contribution of the host galaxy to the light of the optical counterpart of EP241021a, we observed the host galaxy once the light of the transient vanished (see Section 4.6 for more details). We determined that the host contribution is negligible during the majority of the period covered by our light curve. For instance, during the main peak at ∼ 7.7 d, the transient is ≈20, 18, and 13 times brighter than the host in the grz bands, respectively. Meanwhile, at day ∼ 32, the target is brighter by a factor of ≈3.5, 4, and 3.5 for the grz bands, respectively. Only at times beyond day ∼ 70, the photometry of the transient becomes similar to its host galaxy. Nevertheless, we correct the observed photometric data by subtracting the contribution of the host galaxy obtained by the best-fitting galaxy model (see Section 4.6 for more details) in the $ugrizJHK_s$ bands.

3.3 Spectroscopy

We obtained seven optical spectra (see Fig. 3 and Table A5), covering an (observer) wavelength range from ∼3500 to 10 000 Å. The spectra were obtained over the time interval ∼ 3 to 37 d after the X-ray trigger. To quantify the spectral evolution, we fit a power-law function (as $F_\nu \propto \nu^{\beta_{\rm spec}}$) to the data. First, the data were binned using `SpectRes` (A. C. Carnall 2017) to improve the signal-to-noise ratio (at least to have an S/N$\gtrsim$ 5 pixel^{-1}), and masking sky (R. W. Hanuschik 2003) and telluric lines, emission lines of the

[2]To check the consistency of the photometric data at r and R bands, we compute the ratio of the integrated spectra convolved by the transmission functions of both filters. We obtain that the ratio between the r- and R-band fluxes is ∼1.04, i.e. the difference between the flux in both bands is of the order of 4 per cent.

[3]To describe the light curve quantitatively, we fit a three-power-law model to the r-band light curve (the best sampled) in different phases, as $F \propto t^{\alpha}$.

[4]The dead time between exposures is only 7 ms, which is really what allows a search for 'short-time' flares to be done (i.e. there is no chance we missed one due to the CCD readout time being 1–2 min like a normal camera).

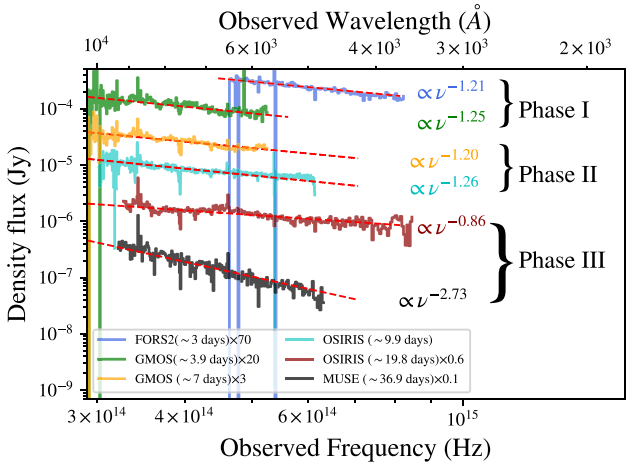

Figure 5. Spectroscopic evolution of EP241021a. The dashed lines depict the power-law model that can describe the continuum of the transient (see Section 3.3 for more details), as well as their best-fitting power-law index. For visual purposes, offsets were applied to the spectra (see the legend).

host (i.e. Hβ, [O II] λ3727, [O III]$\lambda\lambda$4959,5007), and correcting for Galactic extinction using the D. Calzetti et al. (2000) dust model and $E(B-V) = 0.045$ mag (E. F. Schlafly & D. P. Finkbeiner 2011).

During Epoch I, we have two spectral epochs taken by FORS2 (day $\sim$3) and GMOS (day $\sim$3.9), covering the range of $\sim$3500–10 000 Å, with spectral indices of $\beta_{\rm spec} = -1.21 \pm 0.04$ (χ^2/dof = 470.58/491) and -1.25 ± 0.09 (χ^2/dof = 562.41/334), respectively (see Fig. 5). Combining both values, the mean value during Epoch I is $\beta^{\rm I}_{\rm spec} = -1.22 \pm 0.04$. During Epoch II, we have one spectrum taken during the re-brightening at day $\sim$ 7 (GMOS), and two more at day $\sim$ 10 (GMOS & OSIRIS +) at the decay of the main peak. During days $\sim$ 7 and 10, the optical spectral indices are $\beta_{\rm spec} = -1.20 \pm 0.05$ (χ^2/dof = 602.56/396) and -1.26 ± 0.07, respectively. Combining both values, the mean value during Epoch II is $\beta^{\rm II}_{\rm spec} = -1.23 \pm 0.05$, which is compatible with that measured during Epoch I. Overall, until Epoch II, the optical spectra are well described by a power-law function. During Epoch III, we have two spectroscopic observations. On day $\sim$ 19.8 (OSIRIS + spectrum), the best power-law fit is $\beta_{\rm spec} = -0.86 \pm 0.02$ (χ^2/dof = 1179.28/1110), showing a change in the slope with respect to that measured in Epochs I and II. Furthermore, we also used a broken power-law model to explore a potential more complex spectral shape, especially motivated by the flux density peak at $\approx$ 6700 Å (see Fig. 5). We obtained that the broken power-law model (χ^2/dof = 1171.92/1108) depicts red and blue slopes of $\beta^{\rm red}_{\rm spec} = -0.69 \pm 0.09$ and $\beta^{\rm blue}_{\rm spec} = -0.92 \pm 0.04$, respectively, and a break wavelength at $= 6750 \pm 58$ Å. Although the broken power-law model improves the fit, the difference between the models is not statistically significant (the χ^2 decreases by 7.36 for 2 extra d.o.f.). Finally, the last spectrum of EP241021a during Epochs III was taken by MUSE at day $\sim$ 36.9 (see Fig. 5). The spectrum shows an optical spectral index of $\beta_{\rm spec} = -2.73 \pm 0.05$ (χ^2/dof = 480.71/433), which is steeper than the slopes measured in the previous phases, demonstrating a spectral evolution of the transient. Summarizing, the spectral index does not change significantly ($\beta_{\rm spec} \sim -1.2$) until day $\sim$ 20, and it indicates that non-thermal emission dominates until the decay of the main peak; meanwhile, during Epoch III, we have a transition around day $\sim$20, interpretating that either the spectral component changed or a new spectral component emerged.

To investigate if features related to an SN can be detected in any of our spectra, we use the packages GELATO (A. H. Harutyunyan et al. 2008) and SNID (S. Blondin & J. L. Tonry 2007). However, we find no robust evidence for the detection of SN absorption lines in our spectra, which might be a consequence of an additional spectral component that dilutes the equivalent width of the expected absorption lines. This, in combination with the redshift of the event, renders the SN features undetectable to our ground-based 8–10 m telescope observations. We remove any contribution from the host galaxy, given that it is faint (see Section 4.6 for more details).

3.4 Optical-to-X-ray spectral energy distribution

We investigate the evolution of the optical-to-X-ray SED of EP241021a as a function of time using the available photometric data. First, we correct the photometry for Galactic extinction, i.e. $E(B-V) = 0.045$ mag (E. F. Schlafly & D. P. Finkbeiner 2011) using the laws from E. L. Fitzpatrick (1999) and we remove the contribution of the host galaxy (see Section 4.6). We consider time bins with at least four photometric points covering NIR, optical, and/or X-ray wavelengths. Fig. 6 depicts the SED at different time bins. To measure the spectral shape, we fit a power-law function to the optical data (defined by an index $\beta_{\rm op}$) and combine it with the X-ray data (defined by an index $\beta_{\rm ox}$). Considering only the optical data, we get spectral indices weighted mean at Epoch I, and II of $\beta^{\rm I}_{\rm op} = -1.0 \pm 0.1$ and $\beta^{\rm II}_{\rm op} = -1.1 \pm 0.1$, respectively, which both are consistent with our spectroscopic results (see Section 3.3) at 1σ confidence level. Therefore, until day $\sim$20, the SED at optical wavelength does not change significantly, and indicates non-thermal emission dominates (giving its spectral index). Beyond day $\approx$ 18, the SED becomes systematically steeper (even reaching a slope of ≈ -3.1 at day $\sim$37, and confirming the spectroscopic results), which might be interpreted as the emergence of a different spectral component (which is unlikely to be a non-thermal component). The weighted mean of the spectral indices throughout Epoch III is $\beta^{\rm III}_{\rm op} = -1.7 \pm 0.1$. Moreover, the optical spectral index becomes less consistent with the X-ray photon index at late times (see Fig. 6, last three panels from the top).

The index $\beta_{\rm ox}$ remains practically constant during the whole evolution, with spectral index of $\beta_{\rm ox} = -0.92 \pm 0.02$, -1.01 ± 0.01, and -0.94 ± 0.02 for Epochs I, II, and III, respectively. The fact that the $\beta_{\rm op}$ and $\beta_{\rm ox}$ are consistent during Epochs I and II suggests that the same spectral component might be responsible for both energy bands until $\sim$ 20 d. Naturally, the evolution of the optical and X-ray light curves does track each other initially (X-ray data taken by the EP-FXT telescope; X. Shu et al. 2025) until day $\sim$ 20 (G. Gianfagna et al. 2025; X. Shu et al. 2025). However, at late times ($t > 20$ d), it is difficult to reconcile the steepness of the optical spectral index with the X-ray emission, suggesting different spectral components. Given the faint host galaxy (see Section 4.6 for more details), we can discard any influence from the host galaxy to explain this change in $\beta_{\rm op}$ during Epoch III.

3.5 X-ray light curve

In Fig. 7, we show the X-ray light curve of EP241021a as observed with the EP (EP-WXT and EP-FXT instruments; X. Shu et al. 2025), *XMM–Newton* (X. Shu et al. 2025), *Chandra*, and *Swift*-XRT telescopes. As we mentioned before, an approximate peak luminosity

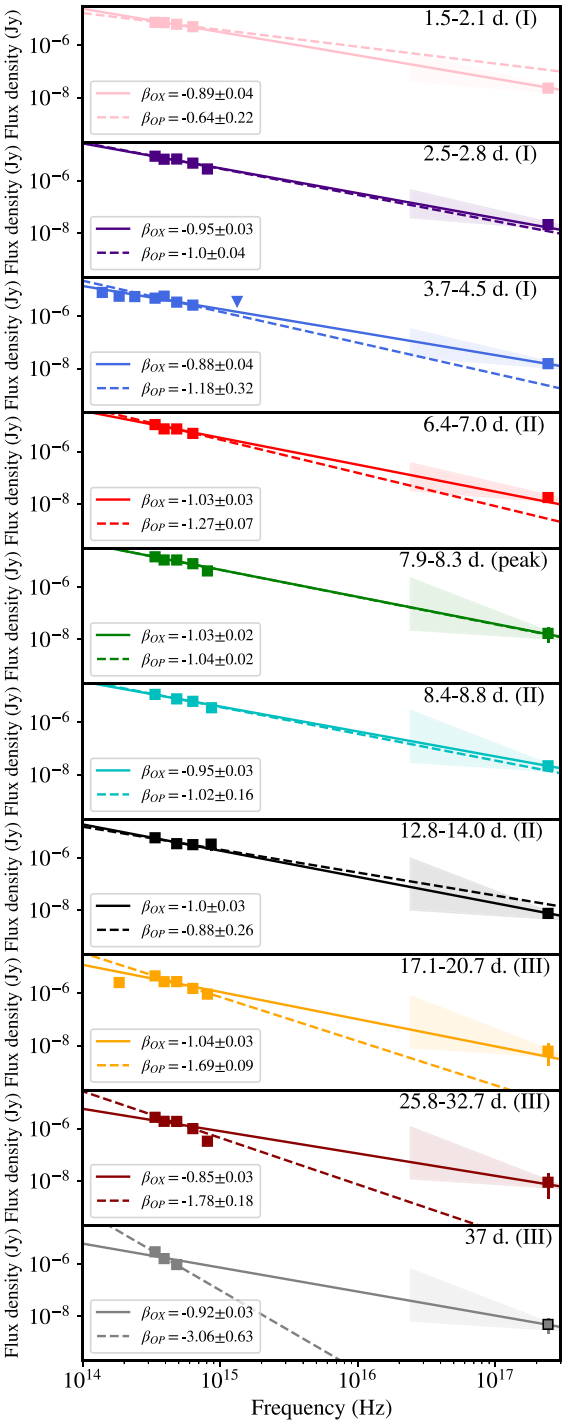

Figure 6. SED of the transient EP241021a at different time bins or epochs (Roman numbers in the top-right corner). We fit a power-law function to the optical data ($F_\nu \propto \nu^\beta$), and to the combined optical to X-ray SED. These fits yield the spectral index $\beta_{\rm op}$ and $\beta_{\rm ox}$, respectively. The uncertainty on the spectral index of a power-law fit to the X-ray spectrum alone is shown as a shaded region. We use the EP-FXT data from X. Shu et al. (2025). The optical and NIR data were corrected for Galactic extinction and for the contribution of the host galaxy.

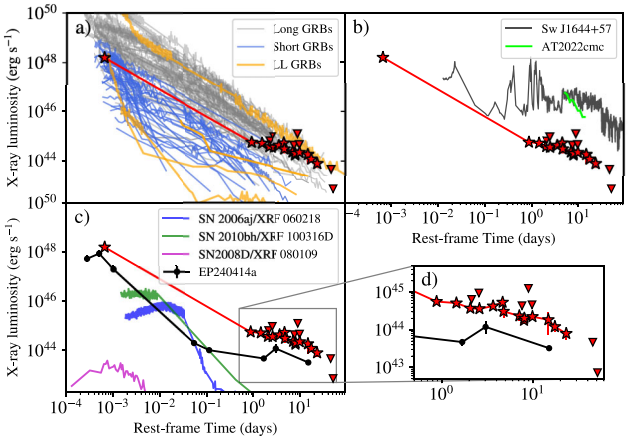

Figure 7. X-ray light curve of FXT EP241021a (stars) in 0.3–10 keV luminosity units combining EP, *XMM–Newton* (X. Shu et al. 2025), *Chandra* (this work), and public *Swift*-XRT data. The inverted triangles depict 3σ upper limits. Each panel depicts a comparison with several individual transients that are overplotted. Panel (a): the X-ray afterglow light curves of 64 LGRBs plus 32 SGRBs and low-luminosity GRBs (P. A. Evans et al. 2007, 2009; M. G. Bernardini et al. 2012; H.-J. Lü et al. 2015); panel (b): the relativistically beamed TDEs Swift J1644+57 (J. S. Bloom et al. 2011; A. J. Levan et al. 2011) and AT2022cmc (I. Andreoni et al. 2022); panel (c): the X-ray flashes XRF 060218/SN 2006aj, XRF 100316D/SN 2010bh (S. Campana et al. 2006; P. A. Evans et al. 2007, 2009; M. Modjaz et al. 2009; R. L. C. Starling et al. 2011; R. Barniol Duran et al. 2015), XRF 080109/SN 2008D (A. M. Soderberg et al. 2008), and the afterglow of the EP transient EP240414a (H. Sun et al. 2025; J. N. D. Dalen et al. 2025); and panel (d): it is a zoom-in of the light curve of EP241021a at late times, with the same units as the other panels.

of EP241021a of $L_{\rm X,peak} \approx 2 \times 10^{48}$ erg s^{-1} is consistent with that of the EP transient EP240414a (see Fig. 7, panel c). Compared with long GRBs (LGRB), the peak luminosity of EP241021a falls in the region occupied by low-luminosity (collapsar) LGRBs (see Fig. 7, panel a); also, this region is populated by short GRBs (SGRB). The peak luminosity is higher by more than two orders of magnitude than that of the X-ray flashes XRF 060 218 and XRF 100316D, and the SBO of SN 2008D (see Fig. 7, panel c). Moreover, the transient at late epochs is brighter than X-ray flashes and even EP240414a by some orders of magnitude, and remains fainter than the relativistically beamed TDEs Swift J1644 + 57 (J. S. Bloom, S. R. Kulkarni & S. G. Djorgovski 2002; A. J. Levan et al. 2011) and AT2022cmc (I. Andreoni et al. 2022) by two orders of magnitude (see Fig. 7, panel b).

The X-ray light curve of EP241021a was fitted using a three-piecewise power-law function by X. Shu et al. (2025). The X-ray light curve at $t \gtrsim 1$ d shows a plateau phase with a power-law index of $-0.28^{+0.17}_{-0.13}$ during days $\sim 1 - 7$, followed by a decline up to 79 d with an index of $-1.16^{+0.30}_{-1.11}$ (see Fig. 7, panel d; X. Shu et al. 2025); then, the transient becomes undetectable by EP-FXT ($\lesssim 2 \times 10^{-14}$ erg cm^{-2} s^{-1}) and even to *XMM–Newton* ($\lesssim 3 \times 10^{-15}$ erg cm^{-2} s^{-1}) around ~ 89 d after the trigger, implying a steeper decay index of $-9.64^{+6.92}_{-7.04}$ at day $33.49^{+10.67}_{-9.72}$ (X. Shu et al. 2025). In addition to these general trends, around day ~ 8 in the observer's frame, the X-ray transient flux increases ($\approx 6 \times 10^{44}$ erg s^{-1}), which coincides with the main peak in the optical light curve (G. Gianfagna et al. 2025). The X-rays at late times fall in a region mostly populated by the afterglow of GRBs, reaching a luminosity of $\approx 5 \times 10^{44}$ erg s^{-1} (see Fig. 7, panel a).

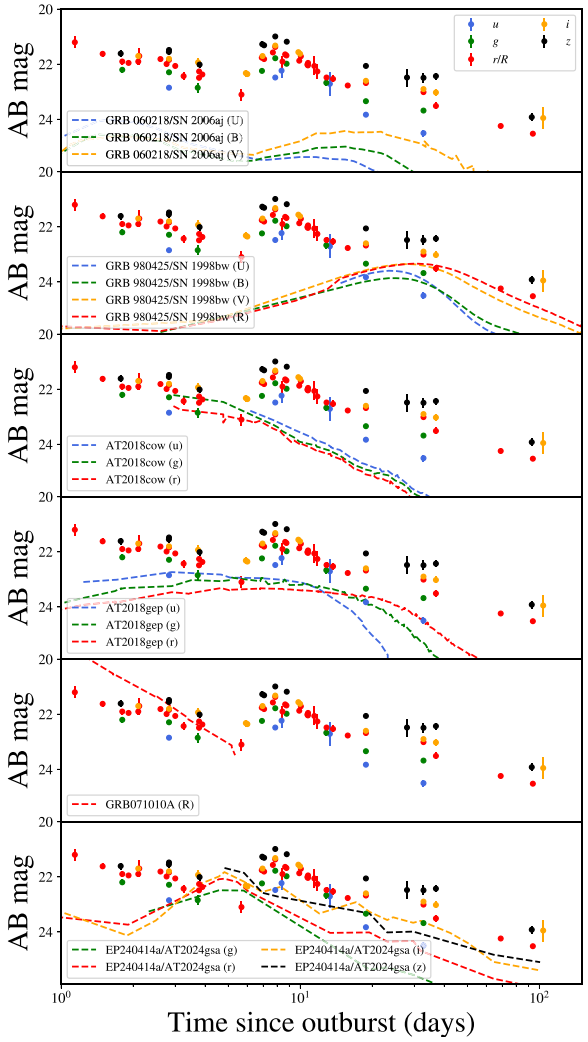

Figure 8. Light curve of FXT EP241021a in the observer frame in different filters ($ugriz$ bands) compared to the light curves of the X-ray flash GRB/XRF 060 218 (first panel; A. M. Soderberg et al. 2006), the prototypical GRB SN Ic-BL SN 1998bw (second panel; F. Patat et al. 2001), the prototypical LFBOT AT2018cow (third panel; S. J. Prentice et al. 2018), the LFBOT AT2018gep (fourth panel; A. Y. Q. Ho et al. 2019), the LGRB 071010A (fifth panel; S. Covino et al. 2008), and the *Einstein Probe* transient EP240414a (sixth panel; J. N. D. Dalen et al. 2025). All the transients were converted to the redshift of EP241021a (i.e. $z = 0.7485$).

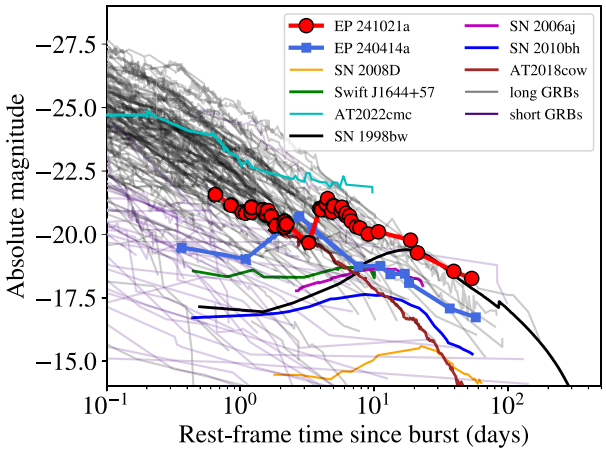

Figure 9. r-band optical light curves of FXT EP241021a (circles) compared to LGRB and SGRB (D. A. Kann, S. Klose & A. Zeh 2006; D. A. Kann et al. 2010, 2011; A. Nicuesa Guelbenzu et al. 2012; D. A. Kann et al. 2024), the SN SBO event XRF 080109/SN 2008D, the X-ray flash source XRF 100316D/SN 2010BH, the LFBOT AT2018cow (D. Xiang et al. 2021), the jetted TDEs AT2022cmc and Swift J1644 + 57 (A. J. Levan et al. 2011; I. Andreoni et al. 2022), and the collapsar FXT EP240414a (J. N. D. Dalen et al. 2025).

4 DISCUSSION

4.1 Light-curve comparison

Fig. 8 shows a comparison between the light curve of EP241021a and several well-known transients, such as GRB 060218/SN 2006aj (A. M. Soderberg et al. 2006), the GRB–SN Ic-BL SN 1998bw (F. Patat et al. 2001), the LFBOT AT2018cow (S. J. Prentice et al. 2018) and candidate LFBOT AT2018gep (A. Y. Q. Ho et al. 2019), and the EP transient EP240414a (J. N. D. Dalen et al. 2025), all shifted to a redshift of $z = 0.7485$.

The double peak of EP241021a is reminiscent of that in the light curve of GRB 060218/SN 2006aj (see Fig. 8, first panel from the top); however, neither the time of the peaks nor the luminosities do not match those observed in EP241021a. Also, the early decay looks consistent with GRB afterglow (see Fig. 8, fifth panel from the top, a comparison with GRB 071010A as an example). Indeed, the power-law index of $\alpha_1 = -0.7 \pm 0.1$ during the first ∼6 d, is consistent with the optical afterglow decay of GRBs (e.g. A. Melandri et al. 2008).

During Epoch II, EP241021a exhibits a rapid re-brightening, peaking around day ∼ 7.7, followed by a power-law decay. From a GRB perspective, re-brightening within the first day is not uncommon in GRB afterglows (e.g. A. Melandri et al. 2008; A. Martin-Carrillo et al. 2014; A. Ugarte Postigo et al. 2018); however, the combination of brightness and time-scale observed in EP241021a is atypical for GRBs, which commonly evolve on time-scales of thousands of seconds. Furthermore, although the prototypical LFBOT AT2018cow and EP241021a differ in their time-scales, the decay rate of EP241021a after the main peak (see Fig. 8, third panel from the top) is very similar to that of AT2018cow ($\sim t^{-2.5}$; R. Margutti et al. 2019). This behaviour is similar to that observed in LFBOT and to the behaviour of EP240414a (see Fig. 8, bottom panel; J. N. D. Dalen et al. 2025). However, the colours of EP241021a are not as blue as the colours observed for LFBOTs (i.e. $g - r < -0.2$ mag; see Fig. A1; A. Y. Q. Ho et al. 2023b).

A mild re-brightening occurred around day ∼ 20 in the r band (also visible perhaps in the z band in M. Busmann et al. 2024), which may result from a combination of multiple components. EP241021a reached an absolute peak magnitude of $M_r \approx -20.1$. Although the high absolute magnitude at this peak is not consistent with that of AT2018gep (which is a target that bridges LFBOTs and SNe Ic-BL; see Fig. 8, fourth panel from the top; T. A. Pritchard et al. 2021), the prototypical SN Ic BL SN 1998bw (with a peak absolute magnitude of $M_R \approx -19.4$ mag; T. J. Galama et al. 1998) matches the late-time evolution of EP241021a reasonably well, especially beyond day ∼ 20 (see Figs 8, second panel from the top).

Finally, Fig. 9 shows a comparison of the r-band optical light curve of EP241021a with various transients (including GRBs, SNe, jetted TDEs, and LFBOTs; D. A. Kann et al. 2006; D. A. Kann et al. 2010, 2011; A. J. Levan et al. 2011; A. Nicuesa Guelbenzu et al. 2012; A. Y. Q. Ho et al. 2019; D. Xiang et al. 2021; J. N. D. Dalen

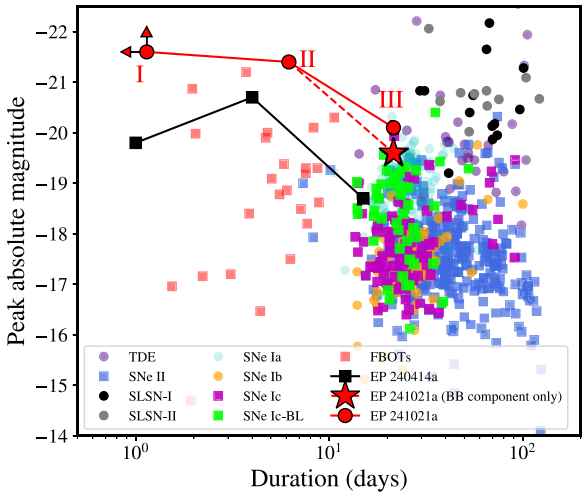

Figure 10. Absolute magnitude at peak versus the duration of transients above half-peak magnitude from the Zwicky Transient Facility Bright Transient Survey (D. A. Perley et al. 2020) such as SN Type Ia, Ib, Ic/BL, and TDEs, and a set of fast transients (AT2018cow-like sources; A. Y. Q. Ho et al. 2023b). The Roman numbers depict the peak emission at each phase of EP241021a. The star represents the absolute magnitude considering only the thermal component (see Section 4.3). Arrows in Epoch I denote limits (see Section 4.2).

et al. 2025). Although the emission $\lesssim 1$ d was missed, Epoch I is brighter than EP240414a, SNe, and AT2018cow. Nevertheless, it lies in a region typically occupied by optically faint LGRBs. The main peak of EP241021a reaches an absolute magnitude similar to brighter optical afterglows; meanwhile, at late times, it remains brighter than typical optical afterglows and eventually matches the decay of SN 1998bw (beyond day ~ 20 rest frame).

To summarize, comparing the light curve of EP241021a with other well-known transients, we identified that different epochs of EP241021a match with various events at different episodes; for instance, at early and late times, EP241021a is more consistent with GRB afterglow and the decay of SN 1998bw, respectively.

4.2 Brightness-duration parameter space

The duration-absolute magnitude diagram is a powerful tool to distinguish between different classes of explosive events. Indeed, different classes of transients populate distinct regions of this parameter space: SNe evolve slowly and have moderate luminosities, GRB afterglows flare briefly but are extremely bright at peak, while TDEs and superluminous supernovae (SLSNe) remain luminous for months (e.g. A. Y. Q. Ho et al. 2023a, fig. 1). We use this diagram to explore the properties of EP241021a (e.g. D. A. Perley et al. 2020; A. Y. Q. Ho et al. 2023a, b), taking into account the evolution of both parameters during its different epochs. We approximate the peak during Epoch I as the earliest detection of the target done by the KAIT telescope (W. Zheng et al. 2024a), i.e. an absolute magnitude of $M_R \lesssim -21.6$ mag with a duration of $\lesssim 1.14$ d. We should keep in mind that the peak could be brighter and the duration shorter. In the case of the main peak during Epoch II at ~ 7.7 days, it reaches a peak absolute magnitude of $M_r \approx -21.4$ mag with a half-flux duration of ≈ 6.2 d (using a broken power-law fitting of the r-band light curve). Finally, the last re-brightening in Epoch III, starting at day $\approx$19, yields an estimated absolute magnitude of $M_r \approx -20.1$ mag and a duration of ≈ 21 d. Fig. 10 shows a comparison of the behaviour of EP241021a (roman numbers label its different epochs) and other transients (e.g. SNe Ia, Ib, Ic/BL, FBOTs, TDEs, and EP240414a) in the duration–absolute magnitude parameter space. Overall, EP241021a has different durations and absolute magnitudes during its different phases. The different episodes place this target in multiple regions in the parameter space. Epoch I might even reside in a region populated by the GRB's afterglow, extrapolating to minutes to hours duration (e.g. see A. Y. Q. Ho et al. 2023a, and its fig. 1). Moreover, the Epoch II falls in a region just covered by FBOTs (A. Y. Q. Ho et al. 2023b); however, it is brighter than the majority of the FBOTs reported by A. Y. Q. Ho et al. (2023b). This could be a consequence of a mixture of spectral components in the emission of the transient.

Furthermore, the re-brightening of EP240414a associated with an SN Type Ic-BL (J. N. D. Dalen et al. 2025) is fainter ($M_r \approx -18.5$ mag) than the peak at Epoch III of EP241021a. The peak of Epoch III falls in a region mainly populated by TDEs, SN Type Ia, and SLSNe. Only a few SNe Ic-BL from the sample (e.g. SN 2021bmf and SN 2023wtq have a peak absolute magnitude of $M_r = -20.6$ and -20.5, respectively; D. A. Perley et al. 2020; A. Aamer et al. 2023; S. Anand et al. 2024) are brighter than EP241021a. Unfortunately, in the case of EP241021a, it was not possible to identify spectroscopic SN features. One possible explanation could be that the added contribution of several non-thermal spectral components masked the SN spectroscopic features (see Section 5). To explore if Epoch III of EP241021a is consistent with SN emission, Fig. A1 shows a colour comparison with four transients: SN 1998bw, AT2018cow, SN 2006aj, and EP240414a. The colours at later epochs look more consistent with SN 1998bw and SN 2006aj than the others. A thermal (SN) contribution might be in line with the steep optical spectral index at day $\sim$37.

4.3 SED analysis

Based on the power-law light curves and optical spectra, and the optical-to-X-ray SED evolution throughout Epochs I and II, it seems likely that both arise from a non-thermal afterglow spectral component. To explore this possibility, firstly, we compare the power-law indices from the optical light curves to those from canonical forward shock models (FS; R. Sari, T. Piran & J. P. Halpern 1999; J. Granot & R. Sari 2002; B. Zhang et al. 2006; H. Gao et al. 2013a). Because the first optical observations of the transient were taken ~ 1.14 d after the trigger, we assume that under the FS model in a deceleration relativistic regime before the jet break, the transient is in the slow-cooling regime. During Epoch I, the decay rate points to an electron energy power-law index $p \approx 2.0 - 2.3$ or $1.4 - 1.7$ in the regime $\nu_a < \nu_m < \nu < \nu_c$ (where ν_a, ν_c, and ν_m are the self-absorption, cooling, and characteristic synchrotron frequencies, respectively) in a constant interstellar medium (ISM) and wind density profile, respectively. Thus, we discard the wind profile due to the electron density of $p < 2$. Taking the derived electron energy index and using the closure relations in the range $\nu_a < \nu_m < \nu < \nu_c$ (H. Gao et al. 2013a), $\beta \sim -0.7$, which is slightly similar to the X-ray-to-optical index derived from the SED (see Fig. 6), supposing that X-ray frequencies are below ν_c. Thus, we can conclude that a non-thermal FS emission is a consistent explanation at this stage. Assuming this non-thermal emission originates from a relativistic jet characterized by an initial Lorentz factor (Γ_0), which decelerates through interaction with the ISM, we estimate Γ_0 based on the premise that the earliest optical detection marks an upper limit on the jet's deceleration time (following the formalism of G. Ghirlanda et al. 2018). For an isotropic-equivalent kinetic energy of $E_0 = 10^{52}$ erg and a uniform ISM density with normalization

parameter of $n_0 = 10$ and 1 cm^{-3} (see Section 5), we derive a lower limit on the initial Lorentz factor of $\Gamma_0 \gtrsim 7 - 9$.

Furthermore, during the decay of the main peak of Epoch II, we find a steeper slope, i.e. $\propto t^{-1.7\pm0.2}$ (excluding the data beyond day ~ 20), where a post-jet-break scenario can be invoked to explain the steeper decay. In the post-jet break regime and in the frequency range of $\nu_a < \nu_m < \nu < \nu_c$ regime, the decay rate is consistent with $\alpha = 3p/4$ (H. Gao et al. 2013a), and the electron density is $p \approx 2.0 - 2.5$ considering an ISM; while in a wind medium $p < 2$, discarding this profile again. On the other hand, the fast rise in the optical light curve from ∼5.6 to 7.7 d ($\propto t^{+3.6}$) cannot be explained based on the FS model, suggesting a more complex mechanism to be at work. Furthermore, from the optical and X-ray SED evolution (see Fig. 6), it is evident that both the optical and the X-ray emission can come from the same spectral component, at least until day $\sim$ 18; nevertheless, at later times, although the X-ray data remain bright until day $\sim$ 40 (X. Shu et al. 2025), their physical origin might be different due to the mismatch of both spectral slopes (see Fig. 6).

To verify a connection with an FS model and data from radio to X-ray wavelengths, we build the SED of the transient at different times using our and public multiwavelength data from the literature: radio ($\gtrsim$ 2 GHz; G. Gianfagna et al. 2025; M. Yadav et al. 2025, see Table A4), optical and NIR (this work; M. Busmann et al. 2025; G. Gianfagna et al. 2025, see Tables A1 and A2), and X-ray (EP-FXT; X. Shu et al. 2025, see Table A3) data. Fig. 11 depicts the SED at six stages, covering Epochs I, II, and III, where the dashed and dotted lines represent the best power-law fit of the optical and radio data, respectively, described by spectral indices $\beta_{\rm op}$ and $\beta_{\rm radio}$.

During days $\sim$ 2.8 and 8.3 (see Fig. 11, first and second panels from the top, respectively), it is clear that extrapolating the $\beta_{\rm op}$ relation to X-ray frequencies is consistent with the observed X-ray flux. However, at day $\sim$ 8.3, extrapolating to lower radio frequencies, it vastly overpredicts the radio emission. Clearly, a break in the power-law extrapolation is needed. Meanwhile, extrapolating the radio power-law SED index ($\beta_{\rm radio} \approx +0.36$) to higher frequencies (optical) also overpredicts the optical flux. This behaviour suggests that the optical and X-ray data can originate from the same spectral component, but it is not obvious that this is also the case for the radio data. We explore whether a single FS model can explain the SED from radio to X-rays. To investigate this possibility, we implement a Markov Chain Monte Carlo (MCMC) method to fit the radio-to-X-ray data of six stages (covering Epochs I, II, and III; see Fig. 11) using a relativistic, isotropic, self-similar decelerating shock model under the slow-cooling regime. In this regime, assuming the convention $F_\nu \propto \nu^\beta$, and defined by the frequencies ν_a, ν_m, and ν_c and the maximum peak flux $F_{\rm max}$, the spectral slopes follow the standard synchrotron slopes as: $\beta = +2, +1/3, -(p-1)/2$, and $-p/2$. Due to the lack of low-frequency radio observations, we fix the self-absorption frequency at $\nu_a \approx 10^9$ Hz (see B. Zhang et al. 2006). As shown by the blue solid lines (posteriors) in the top panel of Fig. 11, the FS model successfully reproduces the SED from optical to X-rays of the transient at day $\sim$ 2.8 (i.e. Epoch I). The best-fitting parameters are: $p = 3.0 \pm 0.2$, $\log(\nu_m) = 12.4^{+0.1}_{-0.3}$, $\log(\nu_c) = 18.2^{+0.8}_{-1.6}$, and peak flux $F_{\rm max} = 2.5^{+0.7}_{-1.1}$ mJy. Moreover, during day $\sim$ 8.3 (see Fig. 11, second panel from the top), the FS model also matches the broad-band SED of the transient, from radio to X-rays. The best-fitting parameters are slightly different with respect to those at the previous stage: $p = 3.0 \pm 0.1$, $\log(\nu_m) = 12.5^{+0.0}_{-0.02}$, $\log(\nu_c) = 17.9^{+1.1}_{-1.2}$, and $F_{\rm max} = 2.6 \pm 0.2$ mJy. Both fits show that afterglow-like emission could explain the entire SED of the transient during Epochs I and II, strengthening the non-thermal nature of the counterpart at both epochs.

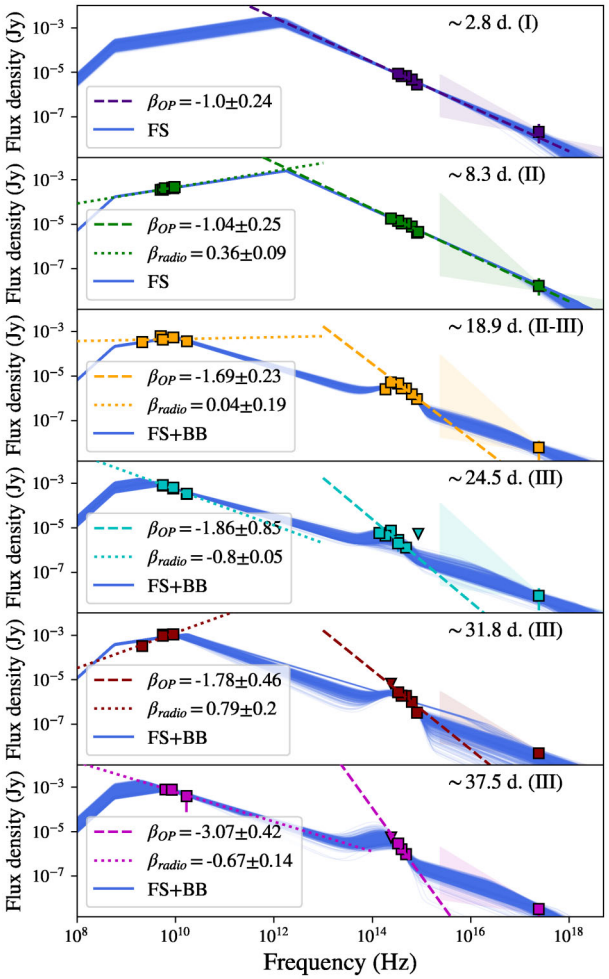

Figure 11. Radio-to-X-ray SED of the transient EP241021a at six different stages. We fit a power-law function to the radio (dotted lines) and optical (dashed lines) data to visualize their trend. Moreover, we fit a more complex model (solid lines) using an MCMC method. In the first and second panels, we fit an FS model in the slow-cooling regime ($\nu_a < \nu_m < \nu_c$, where ν_a, ν_m, and ν_c are the self-absorption, cooling, and characteristic synchrotron frequencies, respectively). In contrast, for the other panels an FS + blackbody (FS + BB) model is fit. The uncertainty on the X-ray spectral index is shown as a shaded region. We use the radio data from G. Gianfagna et al. (2025) and M. Yadav et al. (2025), optical from this work, NIR observations from M. Busmann et al. (2025) and G. Gianfagna et al. (2025), and the EP-FXT data during epoch $\sim$ 32 da from X. Shu et al. (2025). Squares and triangle markers depict detections and upper limits, respectively. The optical and NIR data were corrected for Galactic extinction and for the contribution of the host galaxy.

In the subsequent epochs, we discover (see Fig. 11) that $\beta_{\rm op}$ becomes steeper, and $\beta_{\rm radio}$ shifts to positive values (due to the lack of observation $\gtrsim$ 9 GHz on day $\sim$ 31.8, this transition is not fully resolved). As we demonstrated above, the evolution to a steep spectral index in the optical part of the SED beyond day $\sim$ 20 is incompatible with non-thermal emission (see Fig. 6). If we try to explain the evolution in the SED using a single FS model, we do not obtain a good fit. Furthermore, the slight re-brightening in the optical at $\gtrsim$ 18 d can be explained by the emergence of an additional spectral component. We interpret this new component as blackbody (BB) emission, which can explain the steeper optical spectral index observed at late times (in agreement with the Wien tail of the BB

spectrum), and it also clarifies why the X-ray spectral index differs from that of the optical (see Fig. 6, last three panels from the top). To test this hypothesis, we fit a simple FS model combined with a BB component, described by a temperature and radius $T_{\rm BB}$ and $R_{\rm BB}$, respectively. This combined model is labelled as FS + BB. We expect a transition around days $\sim 18-19$, when the non-thermal component still plays a significant role in the SED. Using the data obtained on day ~ 18.9, we perform fits using both the simple FS model and the FS + BB model, and evaluate their performance using the Bayesian Information Criterion (BIC)[5] Based on the BIC values, we find that the FS + BB model provides a significantly better fit (see Fig. 11, third panel from the top) to the multiwavelength data during day ~ 18.9 ($\rm BIC_{FS} = -134.99$, and $\rm BIC_{FS+BB} = -284.82$).

Extending our analysis to the epochs from approximately ~ 24.5 to 37.5 d (the posteriors are in Table A7), we find that the FS + BB model can simultaneously explain the spectral evolution observed in the radio, optical, and X-ray bands (see Fig. 11). During this observations on Epoch III ($\Delta t \approx 23$ d; see Fig. 11, the last three panels from the top), the BB temperature cools from ~ 9000 to 5300 K, while its bolometric luminosity remains nearly constant at $L_{\rm bol} \sim (1.0-1.4) \times 10^{44}$ erg s^{-1}. Regarding the FS model parameters, we find that $F_{\rm max}$ and ν_c evolve consistently with expectations for a post-jet-break afterglow, i.e. $F_{\rm max} \propto t^{\sim -1}$ and $\nu_c \propto t^{\sim 0}$ (R. Sari et al. 1999), at 95 per cent confidence level. However, the frequency ν_m decays faster than expected: $\nu_m \propto t^{\sim -2.6}$, compared to the standard jet-break model, i.e. $\nu_m \propto t^{-2}$ (R. Sari et al. 1999). This discrepancy could be due to the emergence of additional non-thermal components (see Section 5), indicating to a more complex structure than a unique non-thermal component (which we will also address in Section 5, e.g. R. Filgas et al. 2011; L. Resmi et al. 2012), evolving microphysical parameters (e.g. J. Greiner et al. 2013; K. Varela et al. 2016; M. Marongiu et al. 2022), or variations in the circumburst medium such as density jumps or cavities (e.g. F. A. Harrison et al. 2001; D. Lazzati et al. 2002; Y. F. Huang, K. S. Cheng & Y. Lu 2007; I. Gat, H. van Eerten & A. MacFadyen 2013). Indeed, G. Gianfagna et al. (2025) reported the presence of a second emission component in the radio band (based on the Atacama Large Millimeter/submillimeter Array [ALMA] data at $\sim 10^{11}$ Hz) for EP241021a, first detected around day $\sim 50-70$.

4.4 EP241021a as a tidal disruption event

Based on the high peak X-ray emission of the transient detected by WXT-EP (i.e. $L_{\rm X,peak} \sim 10^{48}$ erg s^{-1}) and its duration (~ 100 s; X. Shu et al. 2025), it is possible that the transient is related to a jetted TDE, which could explain the early non-thermal emission present in the transient. If we compare the X-ray emission of EP241021a and the jetted TDE Sw J1644 + 57 and AT2022cmc (see Fig. 7; J. S. Bloom et al. 2011; A. J. Levan et al. 2011; I. Andreoni et al. 2022). The initial WXT-EP detection is consistent with the early luminosity of Sw J1644 + 57; none the less, after ~ 1 d of the trigger (rest frame), the X-ray emission is fainter than Sw J1644+57 by two orders of magnitude. Furthermore, the light curve of EP241021a does not show evidence for the strong variability detected in Sw J1644 + 57. The jetted TDE AT2022cmc (I. Andreoni et al. 2022) is brighter than EP241021a, and follows a steeper X-ray decay ($\propto t^{-2.1}$; T. Eftekhari et al. 2024) than EP241021a. At optical wavelength, AT2022cmc decays steadily while it remains brighter than EP241021a (see Fig. 9); meanwhile, in the optical range, Sw J16644 + 57 remains fainter than EP241021a (see Fig. 9). Although EP241021a does not follow the same evolution as Sw J1644 + 57 and AT2022cmc, EP241021a might be fully consistent with the large spread in behaviour shown by relativistic TDEs (e.g. O. Teboul & B. D. Metzger 2023; C. Yuan et al. 2025).

Black holes (BH) with masses more than $\sim 10^5$ $\rm M_\odot$ swallow typical WDs whole, and only those of lower mass can produce tidal disruptions of WDs. Many of WD-IMBH TDE systems are also predicted to launch relativistic jets (L. E. Strubbe & E. Quataert 2009; B. A. Zauderer et al. 2011; F. De Colle et al. 2012) as a result of the extremely rapid mass supply (e.g. F. De Colle et al. 2012; J. H. Krolik & T. Piran 2012; R. V. Shcherbakov et al. 2013), powered by rapid IMBH spin (which has been estimated in some IMBH candidates, e.g. S. Wen et al. 2021; Z. Cao et al. 2023) and high magnetic flux (e.g. from a magnetic WD; S. B. Cenko et al. 2012; G. C. Brown et al. 2015; A. Sądowski et al. 2016) via the R. D. Blandford & R. L. Znajek (1977) mechanism. M. MacLeod et al. (2016) show typical peak jet luminosities between $\sim 10^{47} - 10^{50}$ erg s^{-1} and rise time-scales of $\sim 10^2 - 10^4$ s, in agreement with the initial X-ray duration of EP241021a. Under this assumption, the X-ray emission at $\gtrsim 1$ d (rest frame) of 5×10^{44} erg s^{-1} would be related to a thermal accretion disc emission; however, this value is $\sim 1-2$ orders of magnitude higher than the expected Eddington luminosity of a BH with mass $\sim 10^4$ $\rm M_\odot$ (J. Frank, A. King & D. Raine 2002).

Several studies predict a wide diversity of electromagnetic signatures depending on the orbital parameters of the WD–IMBH system. For instance, single, strongly disruptive passages are thought to produce quick-peaking light curves with power-law decay tails as debris slowly falls back to the IMBH (e.g. S. Rosswog, E. Ramirez-Ruiz & W. R. Hix 2009; R. V. Shcherbakov et al. 2013). It has also been suggested that such encounters may result in the WD detonation (S. Rosswog et al. 2009; R. Haas et al. 2012; M. MacLeod et al. 2014), and such a detonations imply that besides emission due to the accretion disc, where a Type Ia-like SN peaking at optical wavelength could be present (e.g. S. Rosswog et al. 2008a; S. Rosswog et al. 2008b; M. MacLeod et al. 2016). Fig. A2 compares the light curve of EP241021a and those predicted from the hydrodynamical simulations of M. MacLeod et al. (2016), who consider a wide range of viewing angles. The optical counterpart of EP241021a is brighter than these predictions, including at later epochs when the thermal component is arising. In addition, the colour evolution of the transient deviates from the predictions of M. MacLeod et al. (2016). Thus, we conclude that EP241021a is not likely to originate from a WD–IMBH TDE where the WD detonated.

4.5 Collapsar origin

The optical colours of the late BB-like emission of EP241021a are similar to those of collapsar events such as SN 1998bw (A. Clocchiatti et al. 2011) and SN 2006aj (S. Campana et al. 2006), suggesting that it might be due to an SN (see Fig. A1). Furthermore, its optical light curve is consistent with the evolution of SN 1998bw beyond day ~ 20 (see Fig. 9). To explore the detectability of a potential SN component, we estimated the brightness of a redshifted SN 1998bw analogue (at $z = 0.7485$ and K-corrected). At $\sim$25 d

[5] $\rm BIC = -2 \ln \mathcal{L} + k \ln N$, where $\mathcal{L}$ is the maximum likelihood of the data, k is the number of model parameters, and N is the number of data points (Ž. Ivezić et al. 2014). We consider the threshold criterion of ΔBIC=$\rm BIC_h$-$\rm BIC_l$>2 to discriminate when comparing two different models, where $\rm BIC_h$ and $\rm BIC_l$ are the higher and lower model BIC, respectively. The larger ΔBIC, the stronger the evidence against the model with a higher BIC is (A. R. Liddle 2007).

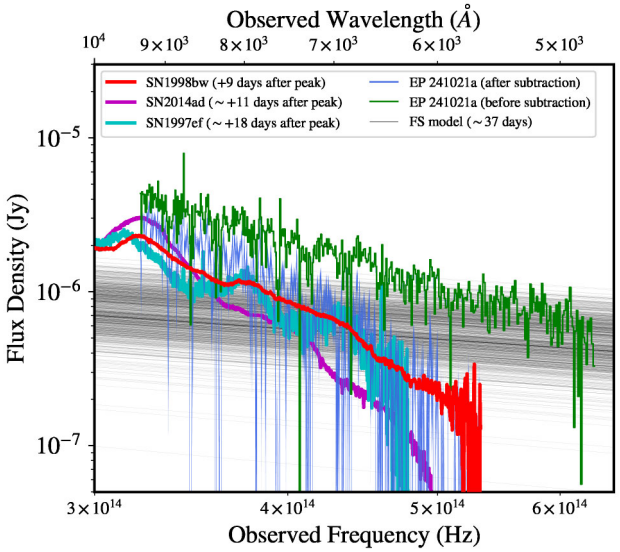

Figure 12. MUSE spectrum of FXT EP241021a before (green) and after (blue) subtracting our best-fitting afterglow model. We show spectra of SN 1998bw (red line; F. Patat et al. 2001) to show that it matches not only the shape but also the overall flux level of our spectrum, and the best-fitting SED at this epoch (see Section 4.3). Moreover, as a comparison of the shape and continuum of the transient, we scaled and overplotted the SN 2014ad and SN 1997ef (M. Modjaz et al. 2014; D. K. Sahu et al. 2018). For comparison, we overplot a random sample of posteriors from the FS model (black lines; see Section 4.3).

after the trigger (≈15 d rest frame), such an event would reach $r \approx 23.6$ mag, whereas EP241021a was observed at $r \approx 22.9$ mag. Therefore, the transient was about twice as luminous as an SN 1998bw-like explosion at the same phase, indicating the presence of an additional component that might dilute the expected broad-lined Type Ic SN absorption lines.

We estimate the contribution of the thermal component to the total emission,[6] at ∼ 18.9 and 37.5 d (i.e. ∼ 10.4 and 21 d rest frame) to be ≈ 50 and 85 per cent, respectively, at r-band frequencies. Therefore, the peak absolute magnitude of the thermal component during Epoch III in the r band is $M_r \approx -19.6$ mag based on a contribution of ≈ 65 per cent during Epoch III. Comparing this value with the absolute magnitude of Type Ic SNe (e.g. see Fig. 10, where the red star depicts the peak absolute magnitude of the thermal contribution), we find that the thermal component by itself is consistent with a Type Ic-BL SN.

Finally, we investigate the MUSE spectrum in detail because during this stage, based on our work, the thermal component contributed ∼ 85 per cent to the total emission, which is higher than the factions determined for the preceding observations. We performed a joint fit of a fixed SN template (SN 1998bw spectrum at day +9 after the peak) scaled to the redshift of EP241021a in combination with an afterglow emission modelled as a power-law model to mimic an SN + non-thermal contribution to the transient. Also, we assume Gaussian noise to emulate the noise level in the MUSE spectrum of EP241021a (corrected by Galactic extinction using the dust model of D. Calzetti et al. 2000). Fig. 12 presents the MUSE spectrum of EP241021a before (green line) and after (blue line) subtracting the best-fitting afterglow component. The best-fitting afterglow has a spectral decay (i.e. $F_\nu \propto \nu^{-0.6}$) consistent with that derived from fitting the SED of the transient (see Fig. 12). We compare our afterglow-subtracted spectrum with the SN 1998bw spectrum (scaled only by the distance; F. Patat et al. 2001), SN 2014ad (D. K. Sahu et al. 2018), and SN 1997ef (M. Modjaz et al. 2014, not only scaled by the distance). Overall, although the S/N of the MUSE spectrum does not allow for identifying SN absorption features, the afterglow-subtracted spectrum is consistent with the spectral shape and continuum of SN 1998bw and other SNe Ic-BL, indicating that the late-time optical counterpart of EP241021a might well be consistent with this type of collapsar transients.

[6]To estimate the contribution of the BB emission to the total emission, we compute the ratio $\int \mathrm{BB}\, d\nu / \int (\mathrm{FS} + \mathrm{BB}) d\nu$, in the frequency range of the r-band.

4.6 Host galaxy properties

To detect the host galaxy of EP241021a, we used HiPERCAM data taken ∼304 d after the X-ray trigger. At that epoch, the light of the transient had vanished. The host galaxy of the transient is extended, and it has a best-fitting position consistent with $\mathrm{RA}_{\mathrm{J2000.0}} = 01^{\mathrm{h}}55^{\mathrm{m}}23^{\mathrm{s}}.44$, $\mathrm{Dec.}_{\mathrm{J2000.0}} = +\,05^{\circ}56'17''.91$. We measure the following photometric points: $m_u = 25.40 \pm 0.23$, $m_g = 24.98 \pm 0.09$, $m_r = 24.38 \pm 0.09$, $m_i = 24.48 \pm 0.17$, and $m_z = 23.43 \pm 0.33$ AB mag. Therefore, the transient's photometry becomes similar to the host galaxy beyond day ∼ 70.

Moreover, the offset between the transient and the centre of the host galaxy is 0.45 arcsec ± 0.67 arcsec (which means a physical offset of 3.39 ± 5.06 kpc) and a chance alignment probability of 0.004. We derive the host properties of EP241021a through the SED fitting of the combined photometry, considering a star formation history (SFH) model described by a delayed exponentially declining function using the package BAGPIPES (A. C. Carnall et al. 2018, 2019). Fig. A3 depicts the best-fitting SED of the available photometric data using BAGPIPES. We obtain a stellar mass, star formation rate (SFR), metallicity, mass-weighted age, and dust attenuation of $\log(\mathrm{M_*/M_\odot}) = 8.6 \pm 0.2$, $\mathrm{SFR} = 2.8^{+1.5}_{-1.1}\ \mathrm{M_\odot\ yr^{-1}}$, $\log(\mathrm{Z/Z_\odot}) = -0.1 \pm 0.3$ (or $12 + \log(\mathrm{O/H}) = 8.6 \pm 0.3$, using M. Asplund et al. 2009), $t_m = 0.07^{+0.14}_{-0.03}$ Gyr, and $\mathrm{A_V} = 1.1 \pm 0.3$, respectively. These results suggest a low-mass, young galaxy with moderate star formation activity, whose metallicity is close to or slightly above solar. Furthermore, it shows a moderate extinction, consistent with active star formation. The high metallicity of the host galaxy is uncommon for the typical LGRB host galaxies (e.g. E. M. Levesque 2014; T. Hashimoto et al. 2015). The model photometry obtained by BAGPIPES is $m_u = 25.21$, $m_g = 25.01$, $m_r = 24.52$, $m_i = 24.23$, $m_z = 23.79$, $m_J = 23.76$, $m_H = 23.40$, and $m_{Ks} = 23.32$ AB mag, used to correct the contribution of the host galaxy to photometry. Small band-to-band differences (e.g. in the u band) are consistent with measurement uncertainties, while the generally brighter measured magnitudes suggest residual transient contribution, thereby justifying the use of the host model photometry for subtraction.

In Fig. 13, we compared the stellar mass (M_*) and specific SFR (sSFR) of EP241021a with other transients such as LGRB and SGRB, CC- and Type Ia SNe, and SLSNe. The cumulative distributions of M_* and sSFR for different transient host populations show that the host of EP241021a lies at relatively low stellar mass, around $\sim 4 \times 10^8\ \mathrm{M_\odot}$, and exhibits a high sSFR of $\sim 9 \times 10^{-9}\ \mathrm{yr^{-1}}$. This combination places the galaxy below the typical stellar masses of Type Ia SNe and fast radio bursts (FRB) hosts, while aligning more closely with the properties of LGRB and SLSN hosts, which are preferentially found in actively star-forming galaxies from moderate to high SFRs. Indeed, LGRBs are preferentially associated with irregular, star-forming, and low-metallicity galaxies, with a few being

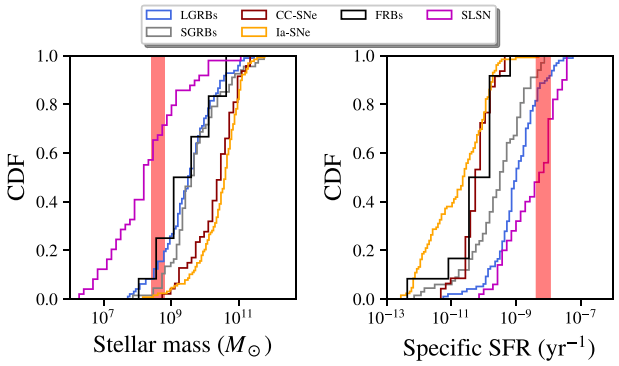

Figure 13. Comparison of the host-galaxy properties of EP241021a at 68 per cent confidence level (vertical region) with the cumulative distributions of stellar mass (left panel) and sSFR (right panel) for LGRBs (P. K. Blanchard, E. Berger & W.-f. Fong 2016; Y. Li, B. Zhang & H.-J. Lü 2016), SGRBs (W. Fong, E. Berger & D. B. Fox 2010; W. Fong et al. 2012, 2014; R. Margutti et al. 2012; E. Berger et al. 2013; T. Sakamoto et al. 2013; W.-f. Fong et al. 2022; A. E. Nugent et al. 2022), FRBs (K. E. Heintz et al. 2020), CC-SNe and Ia-SNe (D. Y. Tsvetkov & O. S. Bartunov 1993; J. L. Prieto, K. Z. Stanek & J. F. Beacom 2008; L. Galbany et al. 2014), and SLSNe (S. Schulze et al. 2021).

spirals with active star formation (A. S. Fruchter et al. 2006; K. Z. Stanek et al. 2006). Their host galaxies are relatively metal-poor compared to the field population (J. P. U. Fynbo et al. 2003; J. X. Prochaska et al. 2004; A. S. Fruchter et al. 2006), favouring a collapsar progenitor model (S. E. Woosley & J. S. Bloom 2006). On the other hand, the formation efficiency of merger-driven transients should be independent of metallicity (M. Chruslinska et al. 2018; N. Giacobbo & M. Mapelli 2018; C. J. Neijssel et al. 2019); indeed, the metallicities of SGRB hosts are significantly higher than those of LGRB hosts (M. Modjaz et al. 2008; E. M. Levesque et al. 2010; E. Berger 2014; E. M. Levesque 2014). This indicates that the EP241021a's environment is characteristic of young, star-forming systems and points toward a massive-star progenitor channel, rather than one associated with older stellar populations, aligned with our previous results.

4.7 Event rate density

In this section, based on the unique properties of EP241021a, such as the lack of gamma-ray counterparts, light-curve evolution, peak X-ray luminosity, and progenitor, we estimate its local event rate density. The estimated local event density (ρ_0) can be derived from (B. B. Zhang et al. 2018; H. Sun et al. 2019):

$$N_{\rm WXT} = \frac{V_{\rm max}\Omega_{\rm WXT}T_{\rm WXT}}{4\pi}\rho_0, \quad (1)$$

where $V_{\rm max}$ represents the maximum volume at which equivalent objects could be detected by EP, $\Omega_{\rm WXT}$ and $T_{\rm WXT}$ depict the EP-WXT FoV (i.e. 3600 sq deg) and on-sky time of the satellite (i.e. $\sim$ 1.5 yr until mid of 2025), respectively, and $N_{\rm WXT}$ is the total number of sources detected (i.e. one event in this case). EP-WXT can detect and identify X-ray transients as faint as $F_{\rm X}\sim10^{-10}$ erg cm^{-2} s^{-1} for a typical exposure time of $\sim$ 200 s. Adopting a peak luminosity of $L_{\rm X}\sim10^{48}$ erg s^{-1} from EP241021a, EP-WXT can then detect similar objects to redshifts up to $z_{\rm max}\sim1.3$. Moreover, following the methodology of H. Sun et al. (2025), the maximum volume $V_{\rm max}$ is

$$V_{\rm max} = \int_0^{z_{\rm max}} \frac{\Omega_{\rm WXT}}{4\pi}\frac{f(z)}{(1+z)}\frac{{\rm d}V(z)}{{\rm d}z}{\rm d}z \quad (2)$$

where, $f(z)$ is a weighted SFH function (taken from P. Madau & M. Dickinson 2014), while ${\rm d}V(z)/{\rm d}z$ is given by

$$\frac{{\rm d}V(z)}{{\rm d}z} = \frac{c}{H_0}\frac{4\pi D_L(z)^2}{(1+z)^2\sqrt{\Omega_M(1+z)^3+\Omega_\Lambda}}, \quad (3)$$

where c, H_0, and D_L are the light speed, *Hubble* constant, and luminosity distance, respectively, while Ω_M and Ω_Λ are matter and dark energy density of our Universe, respectively. In this way, and considering Poissonian uncertainties, we obtained a local event rate density of $\rho_0 \approx 0.23^{+0.34}_{-0.17}$ Gpc^{-3} yr^{-1} at 68 per cent confidence level. Also, if we consider a beaming correction factor of $f_b^{-1} \sim 30$ (where $f_b \simeq \theta_j^2/2$), which corresponds to a mean jet opening angle of $\theta_j \sim 15^\circ$ (see Section 5 for more details), the local event rate density is $\rho_0 \approx 6.9^{+10.2}_{-5.1}$ Gpc^{-3} yr^{-1}. This value is much lower than the rate of other potential extragalactic progenitors of FXTs, such as the merger rate of BNS systems ($\rho_0^{\rm BNS}$=320^{+490}_{-240} Gpc^{-3} yr^{-1}; R. Abbott et al. 2021), low-luminosity LGRBs ($\rho_{0,\rm LL-LGRBs}\sim$150–2100 Gpc^{-3} yr^{-1} (here $f_b^{-1}\sim$1–14 was used; E. Liang et al. 2007; B. Zhang 2018), LGRBs ($\rho_{0,\rm LGRBs}$=40–380 Gpc^{-3} yr^{-1}, using $f_b^{-1}\sim$50–500; D. Wanderman & T. Piran 2010; J. T. Palmerio & F. Daigne 2021), and SGRBs ($\rho_{0,\rm SGRBs}$=45–200 Gpc^{-3} yr^{-1}, using $f_b^{-1}\sim$25–110; D. Guetta & T. Piran 2005; D. Wanderman & T. Piran 2015). Also, our outcome is lower than the FXT-SNe estimation from J. C. Rastinejad et al. (2025). However we should consider our rate density as a lower limit, given the fact that several other FXTs detected by EP have not been classified, and their origin is still unknown. This lower limit is consistent with the millisecond magnetar formation rate from massive stars (S. Biswas et al. 2025). This is an interesting possibility, given that a magnetar engine in EP241021a is an option to explain the rising flux in optical and X-ray bands at day $\sim$8 (see Section 5 for more details).

5 LIGHT-CURVE MODELLING

5.1 Epochs I and II: non-thermal afterglow modelling

To model the light curve, we group the various observations into frequency ranges for a simpler analysis, which we label: $H+J$ (H and J bands); $z+i$ NIR (z and i bands); R for red (R and $r$bands); g for visible (g band); u for UV (u band); and 1 keV for X-ray at 1 keV. These are plotted in the right panel of Fig. 14, with data points represented as dots without uncertainty and upper limits shown as squares with arrows. For the R and 1 keV data, we fit two power-law models, one at $\lesssim$ 6 d (Epoch I) and a second one at $\gtrsim$ 8 d (Epoch II). The power-law indices for these fits are noted within the figure: the early, $\lesssim$ 6 d data at R is $\propto t^{-0.9}$; the early X-ray data are $\propto t^{-0.6}$; the late, $\gtrsim$ 8 d data at R and X-ray is $\propto t^{-1.4}$; while the very late X-ray limit requires $\propto t^{<-3.58}$ after the last detection.

There are different decline indices between optical and X-ray at early times, where the X-ray shows a slower decline than the optical, which is unusual for GRB afterglows (E. Zaninoni et al. 2013). However, if a blastwave decelerates within a wind-like medium, then the X-ray could show such a different temporal decline, where 1 keV $> \nu_c$. For a decline index of $\alpha = -0.6$, the wind medium $\nu > \nu_c$ standard closure relation would require an accelerated electron power-law index of $p \sim 1.47$. None the less, the standard closure relation is not valid for $p < 2$, and the valid solution is unphysical for $\alpha = -0.6$ (H. Gao et al. 2013b). We therefore rule out a wind medium as the origin of the mismatch between the decline index of the optical and X-ray light curves. Figs 6 and 14 indicate an optical to X-ray spectral index $\beta \sim -0.9$. If we apply this to the X-ray data, with 1 keV $> \nu_c$, then the value for $p = 1.8$ gives

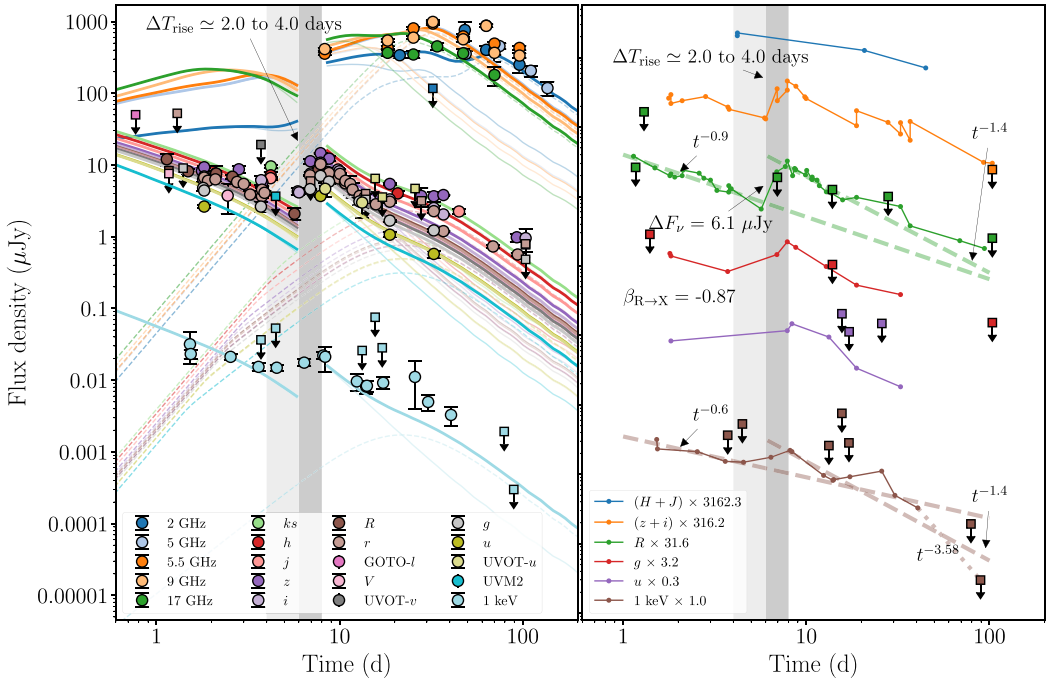

Figure 14. Multiwavelength light-curve modelling of the transient EP241021a. For modelling the multiwavelength light curves, a minimum of three non-thermal components is necessary: (i) at $t \lesssim 7$ d during Epoch I (solid lines), a regular GRB afterglow (optical and X-ray data); (ii) at $t \gtrsim 8$ d during Epoch II (narrow solid lines), a 'regular' GRB afterglow with increased energy relative to the first component, possibly due to rapid energy injection between 6 and 8 d; and (iii) during Epoch III, a very slow component, that begins to contribute significantly to the emission at $t > 10$ d (dashed lines), is responsible for most of the radio afterglow. This component has a Lorentz factor on the order of $\Gamma \approx 3.5$. The dark grey vertical panel indicates the energy injection period for the rapid flux increase, in the r band, while the light grey panel indicates the potential earliest start of the flux increase in other bands.

$\alpha = -0.96$, which is similar to that found using a simple power-law fit to the optical data. For $\nu_m < \nu < \nu_c$, the decline index would be $\alpha = -0.71$. Considering the short time-scale variability in the optical at Epoch I, this value seems more reasonable, although not a precise match to the $t^{-0.9}$ power-law fit to the data in R.

The light-curve discontinuity between ∼6 and 8 d results in a jump in flux, which could for instance be due to energy injection due to a refreshed shock, a jet, or a highly energetic jet core region (that is initially off-axis to the observer) becoming visible, or a patchy shell (where the energy varies randomly across the jet head resulting in 'hotspots' or 'sub-jets'). The duration of the rise is $\Delta T_{\rm rise} \simeq 2$ d and peaks at ∼8 d in the observer frame. The short rise time-scale for the flux increase at 6–8 d violates the expectation for a refreshed shock ($\Delta T > T/4$) or a patchy shell ($\Delta T > T$) (K. Ioka, S. Kobayashi & B. Zhang 2005). An off-axis jet, a patchy shell/sub-jet, or a core region coming into view may be able to explain the rapid rise, however, given the sharp turn-around in the afterglow temporal structure at > 8 d, the angular width of the off-axis jet would have to be extremely narrow (sharpness of the peak) and have a very sharp jet edge (the steepness of the rise). Such conditions are not expected, even in a sub-jet model (T. Nakamura 2000). We therefore do not attempt to model here the details of the short rise time-scale with a physical model, but leave it to future work. However, we point out that at ∼ 4 d post-burst the X-ray afterglow begins to deviate from the steady and continuous decline seen for the optical data in Epoch I (the energy injection time-scale for the afterglow is highlighted within Fig. 14, grey regions).

The spectral index between optical and X-ray at > 10 d is $\beta_{\rm ox} \sim -1$, giving a $p = 2$ for Epoch II. The rapid decline between ∼10–20 d would require a post-jet-break evolution for a $p = 2$, $\beta_{\rm ox} = -1$ SED, yet the late X-ray excess (as well as the radio data) requires a longer-lived component. This may be due to a second energy injection episode, or alternatively, the emission from a wider jet component coming into view.

In Fig. 14 (left panel), we show model light curves that are consistent with the behaviour seen within the data. At < 6 d (Epoch I), we describe the afterglow with a top-hat jet viewed on-axis with an opening angle of $\theta_j \simeq 15.^\circ0$, an isotropic equivalent kinetic energy 6.3×10^{51} erg, an initial Lorentz factor $\Gamma_0 = 100$, and $p = 1.8$ (the microphysical parameters were fixed).[7]

To describe the light curve at > 8 d (Epoch II), we require two components: (i) a late epoch afterglow re-energized copy of the Epoch I model (i.e. afterglow transitions) via some energy injection process, with an isotropic kinetic energy $E_{\rm k,iso} = 2 \times 10^{52}$ erg, and $p = 2.0$, all else as previous (this component is shown as a narrow solid line in Fig. 14, left panel); and (ii) an additional component is required to describe the radio and late X-ray data. To model this, we invoke a sheath, or two-component structure that encases the jet core (this component is shown as a dashed line in Fig. 14, left panel). This sheath extends from the edge of the jet core, at $\theta_j = 15.^\circ0$, to the outer sheath at $\theta_s = 20.^\circ0$. The isotropic equivalent kinetic energy within

[7]The fraction of energy given to electrons $\varepsilon_e = 0.1$, the fraction of energy given to magnetic fields $\varepsilon_B = 0.01$, the participation fraction of electrons in the synchrotron process $\Xi_N = 0.1$, and the ambient density is assumed to be uniform with a number density $n = 10$ cm^{-3} throughout. We use REDBACK afterglow models (N. Sarin et al. 2024), `tophat_redback` and `twocomponent_redback` (with a hollow core) for the afterglow light curves (see G. P. Lamb & S. Kobayashi 2017; G. P. Lamb, I. Mandel & L. Resmi 2018, for details).

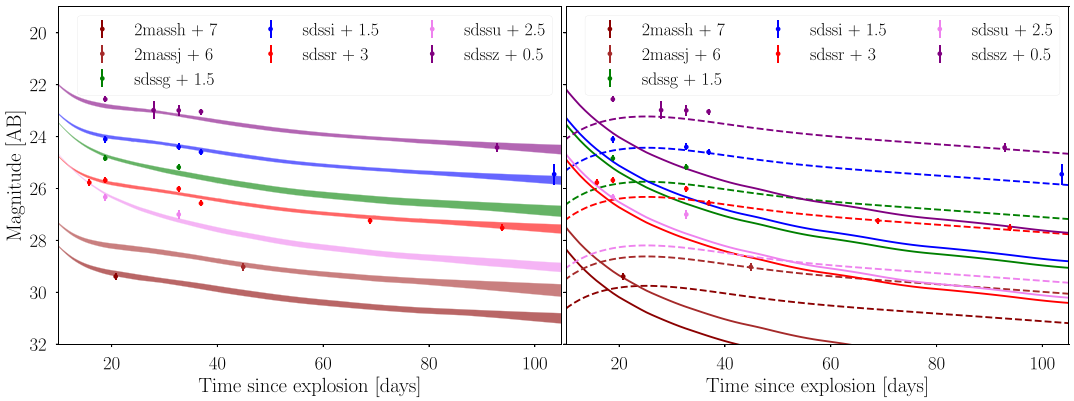

Figure 15. Multiwavelength light-curve modelling of the transient EP241021a beyond day ~ 15. In the left panel, we show 90 per cent credible intervals for different bands from our fit to the optical data with a thermal (one-zone radioactive decay) model combined with two afterglow components. The right-hand panel shows the same data with the SN component (dashed lines) and the afterglow components (solid lines), highlighting how the thermal component begins to dominate after ~ 20 d.

the sheath is $E_{\rm k,iso} = 5 \times 10^{52}$ erg, the Lorentz factor of the sheath material is $\Gamma_{0,s} = 3.5$, and the participation fraction is $\Xi_{N,s} = 0.2$. The total light curve, the sum of the early or late core, respectively, and the sheath, is shown as a thick solid line.

The model light curve fails to reproduce the late X-ray emission at Epoch III. Additionally, the complexity of the radio variability is not exactly reproduced; however, some of this variability may be due to scintillation, which is not modelled. The late optical and IR data during Epoch III appear in excess of the afterglow model – this is expected as the optical and NIR are dominated by an unmodelled thermal component at this time.

5.2 Epoch III: supernova modelling

Drawing motivation from the discussion above (see Section 4), we now consider the origin of the thermal component that begins to dominate the optical emission during Epoch III. To simplify our modelling, we fix the non-thermal emission components as described above and explore the optical light curve post 15 d as a combination of a two non-thermal components (dominating the emission during Epochs I and II) and one thermal component.[8] We first consider TDE-like emission, although we note that no TDE has ever been associated with the highly relativistic outflows (i.e. $\Gamma \approx 100$; e.g. AT2022cmc and Sw J1644 + 57 are modelled to have had $\Gamma \approx 10$; J. S. Bloom et al. 2011; I. Andreoni et al. 2022), which we require to explain the rest of the light curve, as discussed above. This includes both jetted TDE systems where the jet was launched promptly and systems with delayed relativistic outflows relative to optical (Y. Cendes et al. 2024). We consider two models for optical emission from a TDE: (i) the optical luminosity is a function of the fall-back rate onto the BH (J. Guillochon & E. Ramirez-Ruiz 2013; B. Mockler, J. Guillochon & E. Ramirez-Ruiz 2019); and (ii) the optical emission is generated via cooling emission of a hot pressure-supported envelope of the disrupted material (B. D. Metzger 2022; N. Sarin & B. D. Metzger 2024). In general, similar to the models shown in Fig. A2, we find that TDE models (in the relevant BH mass range) do not sufficiently add to the afterglow light curve to explain the thermal component. Moreover, tuning parameters such as the efficiency of the BH to resolve this lead to thermal light curves that last too long, inconsistent with the late-time behaviour seen in EP 241021a.

Next, we consider an SN origin for the thermal component, which, as we discussed, appears to be the likely origin of the thermal component during Epoch III, consistent with the time-scale, luminosity, and colours expected for a Type Ic-BL SN. We attempt four different fits to the data (with the exact setup as above). First, we consider emission from radioactive decay of ^{56}Ni following a one-zone model (W. D. Arnett 1980; D. K. Nadyozhin 1994). Our fits to the overall optical light curve from 15 d is shown in Fig. 15 (left panel), which shows great agreement with the data, and how the SN component (right panel, dashed lines) begins to dominate over the declining afterglow component (right panel, solid lines) at $t \gtrsim 18$ d, consistent with our analysis from the SED. However, while this model broadly works at describing the data, the estimated parameters are in tension with expectations for other Type Ic-BL SNe. In particular, we recover an estimated ejecta mass of $4.7^{+2.6}_{-1.7} {\rm M}_\odot$ with a nickel fraction of $0.5^{+0.3}_{-0.2}$ and extremely high velocities of $\sim 150,000$ km s^{-1}, which are all inconsistent with constraints from other Type Ic (e.g. G. P. Srinivasaragavan et al. 2024).

This discrepancy between our inferred parameters and those of other SNe could be due to several reasons, such as our analysis fixing the components that describe the complex nature of the afterglow. We also perform fits with arbitrarily scaled and shifted SEDs of SN 1998bw, which fail to adequately describe the full light curve. This could raise doubts regarding an SN origin for the thermal component. However, we believe that the high energetics and fast duration of the thermal component in EP241021a compared to other Type Ic-BL SNe (see Fig. 10) suggest another energy source is at play. Such an additional component could also be responsible for the re-brightening in X-rays and optical. To further investigate this scenario, we perform additional fits with models invoking additional energy in an SN from fallback accretion onto a stellar-mass BH (N. Sarin et al. 2024), a millisecond magnetar (N. Sarin et al. 2022; C. M. B. Omand & N. Sarin 2024), and CSM interaction (E. Chatzopoulos, J. C. Wheeler & J. Vinko 2012). We find that all three models provide good fits to the data (with a preference for the magnetar model based on the Bayes factor). Furthermore, the additional energy input from either source also alleviates the concern about our ejecta parameters, for example, across all three models we

[8] We use REDBACK (N. Sarin et al. 2024) implementations of all models and fit for the thermal component using the PYMULTINEST (F. Feroz, M. P. Hobson & M. Bridges 2009; J. Buchner 2016) sampler via BILBY (G. Ashton et al. 2019).

infer ^{56}Ni ≈ 0.15, consistent with expectations and prior constraints from Type Ic SNe (G. P. Srinivasaragavan et al. 2024). Ultimately, which of these interpretations is correct and precise estimates of parameters relies on much more detailed modelling (including the afterglow component in the fit). However, we also stress that the lack of detailed optical data will likely prevent any strong conclusions, as these models are intrinsically uncertain and degenerate. The broad agreement of the data during Epoch III with a combination of two afterglows, SN component plus energy injection, suggests the progenitor of EP241021a is similar to a few other EP FXTs (e.g. J. N. D. Dalen et al. 2025; R. A. J. Eyles-Ferris et al. 2025; J. C. Rastinejad et al. 2025; G. P. Srinivasaragavan et al. 2025), and these events are mostly related to the collapsar phenomena. The exceptional nature of the likely SN in EP241021a points to an additional source of energy besides radioactive decay from ^{56}Ni.

M. Busmann et al. (2025) also modelled their light-curve data for EP241021a with radioactive decay models and included an additional energy input from CSM interaction and magnetar models. Only the former two models are consistent with the implemented physics, as the models we use here, but our inferred parameters are considerably different. For example, they infer an ejecta mass of $9.9\,M_\odot$ with ~ 50 per cent ^{56}Ni for the radioactive-decay only model, entirely inconsistent with any Type Ic SN (G. P. Srinivasaragavan et al. 2024). Similarly, for the CSM interaction with radioactive decay model, they infer a CSM mass of $\approx 95 \pm 60 M_\odot$, implying an extremely massive progenitor. These constraints and discrepancies are most likely driven by the assumptions of the non-thermal afterglow component. We note that our magnetar model is significantly different from the model used in their work, including, for example, losses due to work done by the magnetar wind (see N. Sarin et al. 2022; C. M. B. Omand & N. Sarin 2024, for details) that is ignored in their implementation, so our results are not comparable.

6 CONCLUSIONS

We have presented a detailed multiwavelength study of the FXT EP241021a, discovered on 2024 October 21 by the EP-WXT instrument aboard the *Einstein Probe*. With a redshift of $z = 0.7485$ and a peak X-ray luminosity of $\sim 2 \times 10^{48}$ erg s^{-1}, EP241021a exhibited a rich and complex evolution across the X-ray, optical, NIR, and radio bands over a period of more than $\sim$100 d.

The optical light curve is characterized by a distinct three-phase morphology (see Fig. 4), captured through a smooth triple power-law fit: (I) an initial decay with power-law index $\alpha \approx -0.7$ lasting until day 5.6; (II) a sharp re-brightening peaking at ~ 7.7 d with $\alpha \approx +3.6$, followed by a steeper decay than in the previous phase with a slope of $\alpha \approx -1.3$; and (III) a mild re-brightening around day $\sim$19, followed by a slower decline. This light-curve evolution is not typical of standard GRB afterglows and suggests the presence of multiple physical components contributing to the observed emission.

During the first $\sim$20 d, the optical and X-ray SEDs are both well described by a single non-thermal power law (see Fig. 6), with spectral indices consistent with optically thin synchrotron emission ($\beta_{\rm op} \approx -1.1$ and $\beta_{\rm ox} \approx -1.0$), indicating that the optical and X-ray emission likely originate from the same spectral component. However, beyond day $\sim$20, the optical SED becomes significantly steeper and inconsistent with the X-ray data, reaching a spectral slope of $\beta_{\rm op} \approx -3.1$ (see Fig. 6). Concurrently, the optical source re-brightened, reaching an absolute magnitude of $M_r \approx -20.1$ mag (see Fig. 8).

Spectroscopically, the transient displayed a relatively stable optical continuum with a spectral slope of $\beta_{\rm spec} \approx -1.2$ until day $\sim$19 (see Fig. 5), confirming the photometric evidence of a non-thermal emission component. However, subsequent spectroscopic epochs reveal a different behaviour than in earlier phases, especially our MUSE spectrum shows an even steeper spectral index of $\beta_{\rm spec} \approx -2.73$. This spectral shape is interpreted as due to the emergence of a new emission component. However, no broad absorption lines characteristic of Type Ic-BL SNe were detected.

The inclusion of contemporaneous radio, NIR, optical, and X-ray data from follow-up campaigns (including those presented before in the literature; M. Busmann et al. 2025; G. Gianfagna et al. 2025; X. Shu et al. 2025; M. Yadav et al. 2025) enables broad-band SED fitting (see Fig. 11). Both from analysing our optical data as well as data in the literature, we conclude that a non-thermal origin is required for the early-time emission. However, beyond day $\sim$20, an additional BB component is required to explain the optical SED, alongside the non-thermal contribution. The onset of the re-brightening after day $\gtrsim$20, in combination with the steepening of the optical spectral slope and the evolving SED, is well explained by the emergence of a thermal component. Indeed, the host galaxy does not contribute significantly to the photometry of the transient until after day ≈ 70. This is interpreted as the onset of an SN, supported by its position in the peak absolute magnitude versus duration parameter space (see Fig. 10), its colour evolution (see Fig. A1), and the subtracted-afterglow MUSE spectrum at late times (see Fig. 12). The presence of this thermal component and its consistency with a Type Ic-BL SN signature suggest that the progenitor of this X-ray transient detected by EP might be a collapsar. Our inability to detect typical Type Ic-BL SN features might be caused by the presence of an additional spectral component reducing the equivalent width of the lines, in combination with the relatively high redshift of the event.

We modelled the complex light curve of EP241021a as the superposition of some distinct afterglow components, each representing a separate emission region or energy release episode. The first component, responsible for the early-time decay ($\lesssim$6 d), corresponds to the standard forward-shock afterglow produced by the interaction of a relativistic outflow with the ISM. This model assumes a top-hat jet viewed on-axis, with an opening angle of $\theta_j \approx 15^\circ$, an isotropic-equivalent kinetic energy of 6.3×10^{51} erg, an initial Lorentz factor $\Gamma_0 = 100$, and a power-law index of $p = 1.8$ for the shock-accelerated electrons. This component follows a smooth decline with temporal and spectral indices consistent with synchrotron emission in the slow-cooling regime. To reproduce the light curve beyond $\sim$8 d, two additional components are required. The second component shares characteristics with the first, but incorporates an energy injection episode that increases the kinetic energy by a factor of $\approx$2, while maintaining similar microphysical parameters. A third component, needed to account for the radio and late-time X-ray data, involves a sheath or two-component jet structure surrounding the jet core. In addition, to explain the late-time optical behaviour, an SN component must be included, consistent with the spectrophotometric evidence. This multicomponent framework reinforces the interpretation of EP241021a as a hybrid transient, exhibiting both relativistic jet dynamics and late-time energy sources such as an SN and potential prolonged central engine activity.

EP241021a exemplifies the diverse and evolving population of extragalactic FXTs now being uncovered by the *Einstein Probe* satellite. Its rich multiphase light curve, delayed spectral transition, and ambiguous classification challenge existing models and highlight the importance of early, coordinated, and long-term follow-up across the electromagnetic spectrum.

ACKNOWLEDGEMENTS

JQV, PGJ, JNDD, JSS, MER, and APCH are supported by the European Union (ERC, Starstruck, 101095973, PI: Jonker). Views and opinions expressed are, however, those of the author(s) only and do not necessarily reflect those of the European Union or the European Research Council Executive Agency. Neither the European Union nor the granting authority can be held responsible for them. JQV additionally acknowledges support by the IAU-Gruber foundation.

DMS and MAPT acknowledge support by the Spanish Ministry of Science via the Plan de Generación de conocimiento PID2020-120323GB-I00. DMS also acknowledges support via a Ramon y Cajal Fellowship RYC2023-044941. NS acknowledges support from the Knut and Alice Wallenberg Foundation through the 'Gravity Meets Light' project and the research environment grant 'Gravitational Radiation and Electromagnetic Astrophysical Transients' (GREAT) funded by the Swedish Research Council (VR) under Dnr 2016–06012. GPL is supported by a Royal Society Dorothy Hodgkin Fellowship (grant nos DHF-R1-221175 and DHF-ERE-221005). PTOB acknowledges support from UKRI grant ST/W000857/1. FEB acknowledges support from ANID-Chile BASAL CATA FB210003, FONDECYT Regular 1241005, and Millennium Science Initiative, AIM23-0001. The work of DS was carried out at the Jet Propulsion Laboratory, California Institute of Technology, under a contract with the National Aeronautics and Space Administration (80NM0018D0004).

Based on observations obtained at the international Gemini Observatory (Program IDs GN-2024B-Q-107, GS-2024B-Q-105, and GS-2025A-Q-107), a program of NOIRLab, which is managed by the Association of Universities for Research in Astronomy (AURA) under a cooperative agreement with the National Science Foundation on behalf of the Gemini Observatory partnership: the National Science Foundation (United States), National Research Council (Canada), Agencia Nacional de Investigación y Desarrollo (Chile), Ministerio de Ciencia, Tecnología e Innovación (Argentina), Ministério da Ciência, Tecnologia, Inovações e Comunicações (Brazil), and Korea Astronomy and Space Science Institute (Republic of Korea). Data were processed using the Gemini DRAGONS (Data Reduction for Astronomy from Gemini Observatory North and South) package.

Data for this paper have in part been obtained under the International Time Programme of the CCI (International Scientific Committee of the Observatorios de Canarias of the IAC) with the NOT and GTC operated on the island of La Palma by the Roque de los Muchachos.

The Legacy Surveys consist of three individual and complementary projects: the Dark Energy Camera Legacy Survey (DECaLS; proposal ID no. 2014B-0404; PIs: David Schlegel and Arjun Dey), the Beijing-Arizona Sky Survey (BASS; NOAO Prop. ID no. 2015A-0801; PIs: Zhou Xu and Xiaohui Fan), and the Mayall z-band Legacy Survey (MzLS; Prop. ID no. 2016A-0453; PI: Arjun Dey). DECaLS, BASS, and MzLS together include data obtained, respectively, at the Blanco telescope, Cerro Tololo Inter-American Observatory, NSF's NOIRLab; the Bok telescope, Steward Observatory, University of Arizona; and the Mayall telescope, Kitt Peak National Observatory, NOIRLab. Pipeline processing and analyses of the data were supported by NOIRLab and the Lawrence Berkeley National Laboratory (LBNL). The Legacy Surveys project is honoured to be permitted to conduct astronomical research on Iolkam Duág (Kitt Peak), a mountain with particular significance to the Tohono Oódham Nation.

DATA AVAILABILITY

The data will be available and made public once the paper is published.

REFERENCES

Aamer A. et al., 2023, Transient Name Server AstroNote, 304, 1
Abbott R. et al., 2021, Phys. Rev. X, 11, 021053
Alp D., Larsson J., 2020, ApJ, 896, 39
Anand S. et al., 2024, ApJ, 962, 68
Andersen T., Larsen O. B., Owner-Petersen M., Steenberg K., 1992, in Ulrich M. H., ed., European Southern Observatory Conference and Workshop Proceedings, Vol. 42. European Southern Observatory, p. 311
Andreoni I. et al., 2022, Nature, 612, 430
Appenzeller I. et al., 1998, The Messenger, 94, 1
Arnaud K. A., 1996, in George J., Barnes J. , eds, ASP Conf. Ser. Vol. 101, Astronomical Data Analysis Software and Systems V. Astron. Soc. Pac., San Francisco, p. 17
Arnett W. D., 1980, ApJ, 237, 541
Ashton G., et al., 2019, ApJS, 241, 27
Asplund M., Grevesse N., Sauval A. J., Scott P., 2009, ARA&A, 47, 481
Bacon R. et al., 2010, in McLean I. S., Ramsay S. K., Takami H., eds, Proc. SPIE Conf. Ser.Vol. 7735, Ground-based and Airborne Instrumentation for Astronomy III. SPIE, Bellingham, p. 773508
Barniol Duran R., Nakar E., Piran T., Sari R., 2015, MNRAS, 448, 417
Bauer F. E. et al., 2017, MNRAS, 467, 4841
Berger E., 2014, ARA&A, 52, 43
Berger E. et al., 2013, ApJ, 765, 121
Bernardini M. G., Margutti R., Mao J., Zaninoni E., Chincarini G., 2012, A&A, 539, A3
Biswas S., Jonker P. G., Coleman Miller M., Levan A., Quirola-Vásquez J., 2025, A&A, 700, A161
Blackburn J. K., 1995, in Shaw R. A., Payne H. E., Hayes J. J. E., eds, ASP Conf. Ser.Vol. 77, Astronomical Data Analysis Software and Systems IV. Astron. Soc. Pac., San Francisco, p. 367
Blanchard P. K., Berger E., Fong W.-f., 2016, ApJ, 817, 144
Blandford R. D., Znajek R. L., 1977, MNRAS, 179, 433
Blanton M. R., Roweis S., 2007, AJ, 133, 734
Blondin S., Tonry J. L., 2007, ApJ, 666, 1024
Bloom J. S., Kulkarni S. R., Djorgovski S. G., 2002, AJ, 123, 1111
Bloom J. S. et al., 2011, Science, 333, 203
Bochenek A., Perley D. A., 2024a, GCN Circ., 37869, 1
Bochenek A., Perley D. A., 2024b, GCN Circ., 38030, 1
Bright J. S. et al., 2025, ApJ, 981, 48
Brown G. C., Levan A. J., Stanway E. R., Tanvir N. R., Cenko S. B., Berger E., Chornock R., Cucchiaria A., 2015, MNRAS, 452, 4297
Buchner J., 2016, Astrophysics Source Code Library, record ascl:1606.005
Burns E., Ravasio M. E., Jonker P. G., Goldstein A., Fermi-GBM Team, 2024, GCN Circ., 37855, 1
Busmann M., Gruen D., O'Connor B., Palmese A., Schmidt M., 2024, GCN Circ., 37878, 1
Busmann M. et al., 2025, A&A, 701, A225
Calzetti D., Armus L., Bohlin R. C., Kinney A. L., Koornneef J., Storchi-Bergmann T., 2000, ApJ, 533, 682
Campana S. et al., 2006, Nature, 442, 1008
Cao Z., Jonker P. G., Wen S., Stone N. C., Zabludoff A. I., 2023, MNRAS, 519, 2375
Cardiel N. et al., 2019, in Teuben P. J., Pound M. W., Thomas B. A., Warner E. M., eds, ASP Conf. Ser.Vol. 523, Astronomical Data Analysis Software and Systems XXVII. Astrono. Soc. Pac., San Francisco, p. 317
Carnall A. C., 2017, preprint (arXiv:1705.05165)
Carnall A. C., McLure R. J., Dunlop J. S., Davé R., 2018, MNRAS, 480, 4379

Carnall A. C., Leja J., Johnson B. D., McLure R. J., Dunlop J. S., Conroy C., 2019, ApJ, 873, 44
Cash W., 1979, ApJ, 228, 939
Cendes Y., et al., 2024, ApJ, 971, 185
Cenko S. B. et al., 2012, ApJ, 753, 77
Cepa J. et al., 2000, in Iye M., Moorwood A. F., eds, Proc. SPIE Conf. Ser.Vol. 4008, Optical and IR Telescope Instrumentation and Detectors. SPIE, Bellingham, p. 623
Chatzopoulos E., Wheeler J. C., Vinko J., 2012, ApJ, 746, 121
Chruslinska M., Belczynski K., Klencki J., Benacquista M., 2018, MNRAS, 474, 2937
Clemens J. C., Crain J. A., Anderson R., 2004, in Moorwood A. F. M., Iye M., eds, Proc. SPIE Conf. Ser.Vol. 5492, Ground-based Instrumentation for Astronomy. SPIE, Bellingham, p. 331
Clocchiatti A., Suntzeff N. B., Covarrubias R., Candia P., 2011, AJ, 141, 163
Covino S. et al., 2008, MNRAS, 388, 347
Dai Z. G., Wang X. Y., Wu X. F., Zhang B., 2006, Science, 311, 1127
De Colle F., Guillochon J., Naiman J., Ramirez-Ruiz E., 2012, ApJ, 760, 103
De Luca A. et al., 2021, A&A, 650, A167
de Ugarte Postigo A. et al., 2018, A&A, 620, A190
Dhillon V. S. et al., 2021, MNRAS, 507, 350
Eappachen D. et al., 2022, MNRAS, 514, 302
Eappachen D. et al., 2023, ApJ, 948, 91
Eappachen D. et al., 2024, MNRAS, 527, 11823
Eftekhari T. et al., 2024, ApJ, 974, 149
Erben T. et al., 2005, Astron. Nachr., 326, 432
ESO CPL Development Team, 2015, Astrophysics Source Code Library, record ascl:1504.003
Evans P. A. et al., 2007, A&A, 469, 379
Evans P. A. et al., 2009, MNRAS, 397, 1177
Evans P. A., Page K. L., Beardmore A. P., Eyles-Ferris R. A. J., Osborne J. P., Campana S., Kennea J. A., Cenko S. B., 2023, MNRAS, 518, 174
Eyles-Ferris R. A. J. et al., 2025, ApJ, 988, L14
Feroz F., Hobson M. P., Bridges M., 2009, MNRAS, 398, 1601
Filgas R. et al., 2011, A&A, 526, A113
Fitzpatrick E. L., 1999, PASP, 111, 63
Fong W., Berger E., Fox D. B., 2010, ApJ, 708, 9
Fong W. et al., 2012, ApJ, 756, 189
Fong W. et al., 2014, ApJ, 780, 118
Fong W.-f. et al., 2022, ApJ, 940, 56
Frank J., King A., Raine D., 2002, Accretion Power in Astrophysics, 3rd edn. Cambridge Univ. Press, Cambridge
Freeburn J., Andreoni I., Quirola-Vasquez J., Malesani D. B., Bauer F. E., Jonker P. G., 2024, GCN Circ., 37911, 1
Freeman P. E., Kashyap V., Rosner R., Lamb D. Q., 2002, ApJS, 138, 185
Freudling W., Romaniello M., Bramich D. M., Ballester P., Forchi V., García-Dabló C. E., Moehler S., Neeser M. J., 2013, A&A, 559, A96
Fruchter A. S. et al., 2006, Nature, 441, 463
Fruscione A. et al., 2006, in Silva D. R., Doxsey R. E., eds, Proc. SPIE Conf. Ser.Vol. 6270, Observatory Operations: Strategies, Processes, and Systems. SPIE, Bellingham, p. 62701V
Fu S. Y., Zhu Z. P., An J., Jiang S. Q., Liu X., Xu D., Fynbo J. P. U., Turkki M., 2024a, GCN Circ., 37840, 1
Fu S. Y. et al., 2024b, GCN Circ., 37842, 1
Fynbo J. P. U. et al., 2003, A&A, 406, L63
Galama T. J. et al., 1998, Nature, 395, 670
Galbany L. et al., 2014, A&A, 572, A38
Gao H., Lei W.-H., Zou Y.-C., Wu X.-F., Zhang B., 2013a, New Astron. Rev., 57, 141
Gao H., Ding X., Wu X.-F., Zhang B., Dai Z.-G., 2013b, ApJ, 771, 86
Garmire G. P., 1997, in American Astronomical Society Meeting Abstracts #190, p. 34.04
Garzón F. et al., 2022, A&A, 667, A107
Gat I., van Eerten H., MacFadyen A., 2013, preprint (arXiv:1308.4885)
Gehrels N. et al., 2004, ApJ, 611, 1005
Ghirlanda G. et al., 2018, A&A, 609, A112
Giacobbo N., Mapelli M., 2018, MNRAS, 480, 2011
Gianfagna G. et al., 2025, A&A, 703, A92
Gillanders J. H. et al., 2024, ApJ, 969, L14
Gimeno G. et al., 2016, in Evans C. J., Simard L., Takami H., eds, Proc. SPIE Conf. Ser.Vol. 9908, Ground-based and Airborne Instrumentation for Astronomy VI. SPIE, Bellingham, p. 99082S
Glennie A., Jonker P. G., Fender R. P., Nagayama T., Pretorius M. L., 2015, MNRAS, 450, 3765
Granot J., Sari R., 2002, ApJ, 568, 820
Greiner J. et al., 2013, A&A, 560, A70
Guetta D., Piran T., 2005, A&A, 435, 421
Guillochon J., Ramirez-Ruiz E., 2013, ApJ, 767, 25
Haas R., Shcherbakov R. V., Bode T., Laguna P., 2012, ApJ, 749, 117
Hanuschik R. W., 2003, A&A, 407, 1157
Harrison F. A. et al., 2001, ApJ, 559, 123
Harutyunyan A. H. et al., 2008, A&A, 488, 383
Hashimoto T., Perley D. A., Ohta K., Aoki K., Tanaka I., Niino Y., Yabe K., Kawai N., 2015, ApJ, 806, 250
Heintz K. E. et al., 2020, ApJ, 903, 152
Heise J., in't Zand J., 2010, in Compact Stellar X-ray Sources. Cambridge Univ. Press, Cambridge, p. 267
Ho A. Y. Q. et al., 2019, ApJ, 887, 169
Ho A. Y. Q. et al., 2023a, Nature, 623, 927
Ho A. Y. Q. et al., 2023b, ApJ, 949, 120
Hook I. M., Jørgensen I., Allington-Smith J. R., Davies R. L., Metcalfe N., Murowinski R. G., Crampton D., 2004, PASP, 116, 425
Hu J. W., Wang Y., He H., Yang S. K., Cheng Y. H., Yuan W. M., Einstein Probe Team, 2024, GCN Circ., 37834, 1
Huang Y. F., Cheng K. S., Lu Y., 2007, Adv. Space Res., 40, 1214
Ingham J., Arnaud K., 2006, NASA/GSFC HEASARC. Greenbelt, MD
Ioka K., Kobayashi S., Zhang B., 2005, ApJ, 631, 429
Irwin J. A. et al., 2016, Nature, 538, 356
Ivezić Ž., Connolly A. J., VanderPlas J. T., Gray A., 2014, Statistics, Data Mining, and Machine Learning in Astronomy. Princeton Univ. Press, Princeton
J-Jin J., Mu H. Y., F Z., Sun Y. G., Mao R. W. Y. M., 2024, GCN Circ., 37892, 1
Jiang S.-Q. et al., 2025, ApJ, 988, L34
Jonker P. G. et al., 2013, ApJ, 779, 14
Jonker P. G. et al., 2026, MNRAS, 545, staf2021
Kalberla P. M. W., Haud U., 2015, A&A, 578, A78
Kalberla P. M. W., Burton W. B., Hartmann D., Arnal E. M., Bajaja E., Morras R., Pöppel W. G. L., 2005, A&A, 440, 775
Kann D. A., Klose S., Zeh A., 2006, ApJ, 641, 993
Kann D. A. et al., 2010, ApJ, 720, 1513
Kann D. A. et al., 2011, ApJ, 734, 96
Kann D. A. et al., 2024, A&A, 686, A56
Krolik J. H., Piran T., 2012, ApJ, 749, 92
Kumar A., Maund J. R., Sun N. C., Li W. X., Wang Y. N., Wiersema K., 2024, GCN Circ., 37875, 1
Labrie K. et al., 2023a, DRAGONS, Zenodo, https://doi.org/10.5281/zenodo.7776065
Labrie K. et al., 2023b, Res. Notes AAS, 7, 214
Lamb G. P., Kobayashi S., 2017, MNRAS, 472, 4953
Lamb G. P., Mandel I., Resmi L., 2018, MNRAS, 481, 2581
Lang D., Hogg D. W., Mierle K., Blanton M., Roweis S., 2010, AJ, 139, 1782
Lazzati D., Rossi E., Covino S., Ghisellini G., Malesani D., 2002, A&A, 396, L5
Levan A. J. et al., 2011, Science, 333, 199
Levan A. J. et al., 2025, Nature Astronomy,1375–1386,
Levesque E. M., 2014, PASP, 126, 1
Levesque E. M., Kewley L. J., Berger E., Zahid H. J., 2010, AJ, 140, 1557
Li W. X. et al., 2024a, GCN Circ., 37844, 1
Li W. X., Sun N. C., Maund J., Wang Y. N., Wiersema K., 2024b, GCN Circ., 37846, 1
Li W. X. et al., 2025, preprint (arXiv:2504.17034)
Li Y., Zhang B., Lü H.-J., 2016, ApJS, 227, 7
Liang E., Zhang B., Virgili F., Dai Z. G., 2007, ApJ, 662, 1111
Liddle A. R., 2007, MNRAS, 377, L74
Lin D., Irwin J. A., Berger E., Nguyen R., 2022, ApJ, 927, 211

Lü H.-J., Zhang B., Lei W.-H., Li Y., Lasky P. D., 2015, ApJ, 805, 89
MacLeod M., Goldstein J., Ramirez-Ruiz E., Guillochon J., Samsing J., 2014, ApJ, 794, 9
MacLeod M., Guillochon J., Ramirez-Ruiz E., Kasen D., Rosswog S., 2016, ApJ, 819, 3
Madau P., Dickinson M., 2014, ARA&A, 52, 415
Maguire K., Eracleous M., Jonker P. G., MacLeod M., Rosswog S., 2020, Space Sci. Rev., 216, 39
Margutti R. et al., 2012, ApJ, 756, 63
Margutti R. et al., 2019, ApJ, 872, 18
Marongiu M. et al., 2022, A&A, 658, A11
Martin-Carrillo A. et al., 2014, A&A, 567, A84
McLean I. S. et al., 2012, in McLean I. S., Ramsay S. K., Takami H., eds, Proc. SPIE Conf. Ser.Vol. 8446, Ground-based and Airborne Instrumentation for Astronomy IV. SPIE, Bellingham, p. 84460J
Melandri A. et al., 2008, ApJ, 686, 1209
Metzger B. D., 2022, ApJ, 937, L12
Metzger B. D., Quataert E., Thompson T. A., 2008, MNRAS, 385, 1455
Mockler B., Guillochon J., Ramirez-Ruiz E., 2019, ApJ, 872, 151
Modjaz M. et al., 2008, in Bresolin F., Crowther P. A., Puls J., eds, IAU Symp.Vol. 250, Massive Stars as Cosmic Engines. International Astronomical Union, p. 503
Modjaz M. et al., 2009, ApJ, 702, 226
Modjaz M. et al., 2014, AJ, 147, 99
Moskvitin A. S., Spiridonova O. I., GRB follow-up Team, 2024a, GCN Circ., 37850, 1
Moskvitin A. S., Spiridonova O. I., GRB follow-up Team, 2024b, GCN Circ., 37910, 1
Moskvitin A. S., Spiridonova O. I., GRB follow-up Team, 2024c, GCN Circ., 37951, 1
Nadyozhin D. K., 1994, ApJS, 92, 527
Nakamura T., 2000, ApJ, 534, L159
Neijssel C. J. et al., 2019, MNRAS, 490, 3740
Nicuesa Guelbenzu A. et al., 2012, A&A, 548, A101
Novara G. et al., 2020, ApJ, 898, 37
Nugent A. E. et al., 2022, ApJ, 940, 57
O'Connor B. et al., 2025, ApJ, 979, L30
Omand C. M. B., Sarin N., 2024, MNRAS, 527, 6455
Ott T., 2012, Astrophysics Source Code Library, record ascl:1210.019
Palmerio J. T., Daigne F., 2021, A&A, 649, A166
Pan Y. et al., 2024, GCN Circ., 37968, 1
Pascual S., Gallego J., Cardiel N., Eliche-Moral M. C., 2010, in Mizumoto Y., Morita K. I., Ohishi M., eds, ASP Conf. Ser.Vol. 434, Astronomical Data Analysis Software and Systems XIX. Astron. Soc. Pac., San Francisco, p. 353
Patat F. et al., 2001, ApJ, 555, 900
Pérez-Fournon I. et al., 2024, GCN Circ., 37858, 1
Perley D. A. et al., 2020, ApJ, 904, 35
Pessa I., Tejos N., Moya C., 2018, preprint (arXiv:1803.05005)
Prentice S. J. et al., 2018, ApJ, 865, L3
Prieto J. L., Stanek K. Z., Beacom J. F., 2008, ApJ, 673, 999
Pritchard T. A. et al., 2021, ApJ, 915, 121
Prochaska J. X. et al., 2004, ApJ, 611, 200
Pugliese G. et al., 2024, GCN Circ., 37852, 1
Quirola-Vásquez J. et al., 2022, A&A, 663, A168
Quirola-Vásquez J. et al., 2023, A&A, 675, A44
Quirola-Vasquez J. A., Malesani D. B., Levan A. J., Bauer F. E., Jonker P. G., 2024a, GCN Circ., 37930, 1
Quirola-Vásquez J. et al., 2024b, A&A, 683, A243
Quirola-Vásquez J. et al., 2025, A&A, 695, A279
Rastinejad J. C. et al., 2025, ApJ, 988, L13
Resmi L. et al., 2012, MNRAS, 427, 288
Ror A. K., Gupta A., Tripathi T., Pandey S. B., Mishra K., 2024, GCN Circ., 37845, 1
Rosswog S., Ramirez-Ruiz E., Hix W. R., Dan M., 2008a, Comput. Phys. Commun., 179, 184
Rosswog S., Ramirez-Ruiz E., Hix W. R., 2008b, ApJ, 679, 1385
Rosswog S., Ramirez-Ruiz E., Hix W. R., 2009, ApJ, 695, 404
Sądowski A., Tejeda E., Gafton E., Rosswog S., Abarca D., 2016, MNRAS, 458, 4250
Sahu D. K., Anupama G. C., Chakradhari N. K., Srivastav S., Tanaka M., Maeda K., Nomoto K., 2018, MNRAS, 475, 2591
Sakamoto T. et al., 2013, ApJ, 766, 41
Sari R., Piran T., Halpern J. P., 1999, ApJ, 519, L17
Sarin N., Metzger B. D., 2024, ApJ, 961, L19
Sarin N., Omand C. M. B., Margalit B., Jones D. I., 2022, MNRAS, 516, 4949
Sarin N. et al., 2024, MNRAS, 531, 1203
Schirmer M., 2013, ApJS, 209, 21
Schlafly E. F., Finkbeiner D. P., 2011, ApJ, 737, 103
Schneider B., Adami C., 2024, GCN Circ., 38022, 1
Schulze S. et al., 2021, ApJS, 255, 29
Science Software Branch at STScI, 2012, Astrophysics Source Code Library, record ascl:1207.011
Scully B., Matzner C. D., Yalinewich A., 2023, MNRAS, 525, 1562
Shcherbakov R. V., Pe'er A., Reynolds C. S., Haas R., Bode T., Laguna P., 2013, ApJ, 769, 85
Shu X. et al., 2025, ApJ, 990, L29
Soderberg A. M. et al., 2006, Nature, 442, 1014
Soderberg A. M. et al., 2008, Nature, 454, 246
Soto K. T., Lilly S. J., Bacon R., Richard J., Conseil S., 2016, MNRAS, 458, 3210
Srinivasaragavan G. P. et al., 2024, ApJ, 976, 71
Srinivasaragavan G. P. et al., 2025, ApJ, 988, L60
Srivastav S. et al., 2025, ApJ, 978, L21
Stanek K. Z. et al., 2006, Acta Astron., 56, 333
Starling R. L. C. et al., 2011, MNRAS, 411, 2792
Strubbe L. E., Quataert E., 2009, MNRAS, 400, 2070
Sun H., Zhang B., Gao H., 2017, ApJ, 835, 7
Sun H., Li Y., Zhang B.-B., Zhang B., Bauer F. E., Xue Y., Yuan W., 2019, ApJ, 886, 129
Sun H. et al., 2022, ApJ, 927, 224
Sun H. et al., 2025, Nat. Astron., 9, 1073
Teboul O., Metzger B. D., 2023, ApJ, 957, L9
Tody D., 1986, in Crawford D. L., ed., Proc. SPIE Conf. Ser.Vol. 627, Instrumentation in Astronomy VI. SPIE, Bellingham, p. 733
Tsvetkov D. Y., Bartunov O. S., 1993, Bull. Inf. Cent. Donnees Stellaires, 42, 17
van Dalen J. N. D. et al., 2025, ApJ, 982, L47
van Dokkum P. G., 2001, PASP, 113, 1420
Varela K. et al., 2016, A&A, 589, A37
Wanderman D., Piran T., 2010, MNRAS, 406, 1944
Wanderman D., Piran T., 2015, MNRAS, 448, 3026
Wang Y., He H., Yang S. K., Cheng Y. H., Hu J. W., Xu X. P., Yuan W., Einstein Probe Team, 2024, GCN Circ., 37848, 1
Waxman E., Katz B., 2017, in Alsabti A. W., Murdin P., eds, Handbook of Supernovae. Springer International Publishing AG, Cham, p. 967
Weilbacher P. M. et al., 2020, A&A, 641, A28
Wen S., Jonker P. G., Stone N. C., Zabludoff A. I., 2021, ApJ, 918, 46
Willingale R., Starling R. L. C., Beardmore A. P., Tanvir N. R., O'Brien P. T., 2013, MNRAS, 431, 394
Woosley S. E., Bloom J. S., 2006, ARA&A, 44, 507
Wu G.-L. et al., 2025, ApJ, 991, 115
Xiang D. et al., 2021, ApJ, 910, 42
Xue Y. Q. et al., 2019, Nature, 568, 198
Yadav M. et al., 2025, ApJ, 995, 216
Yu Y.-W., Zhang B., Gao H., 2013, ApJ, 776, L40
Yuan C., Winter W., Zhang B. T., Murase K., Zhang B., 2025, ApJ, 982, 196
Yuan W. et al., 2015, preprint (arXiv:1506.07735)
Yuan W., Zhang C., Chen Y., Ling Z., 2022, preprint (arXiv:2209.09763)
Yuan W. et al., 2025, Sci. China Phys. Mech. Astron., 68, 239501
Zaninoni E., Bernardini M. G., Margutti R., Oates S., Chincarini G., 2013, A&A, 557, A12
Zauderer B. A. et al., 2011, Nature, 476, 425
Zhang B. B. et al., 2018, Nat. Commun., 9, 447
Zhang B., 2013, ApJ, 763, L22

Zhang B., 2018, The Physics of Gamma-Ray Bursts. Cambridge Univ. Press, Cambridge
Zhang B., Fan Y. Z., Dyks J., Kobayashi S., Mészáros P., Burrows D. N., Nousek J. A., Gehrels N., 2006, ApJ, 642, 354
Zheng J.-H., Zhu J.-P., Lu W., Zhang B., 2025, ApJ, 985, 21
Zheng W., Han X., Zhang P., Filippenko V. A., KAIT GRB team, 2024a, GCN Circ., 37849, 1
Zheng W., Brink T. G., Filippenko A. V., Yang Y., KAIT GRB Team, 2024b, GCN Circ., 38294, 1

APPENDIX A: COMPARISON WITH OTHER TRANSIENTS

As we mentioned above, the comparison with well-known transients is essential to discover the progenitor of EP241021a. Fig. A1 depicts the colour evolution of EP241021a, and a comparison with transients such as SN 1998bw (A. Clocchiatti et al. 2011), AT2018cow (S. J. Prentice et al. 2018), SN 2006aj (A. M. Soderberg et al. 2006), and EP240414a (J. N. D. Dalen et al. 2025). Meanwhile, Fig. A2 shows the optical multiband light curves of EP241021a and the hydrodynamical simulation developed by M. MacLeod et al. (2016) for the tidal disruption of WD by IMBH.

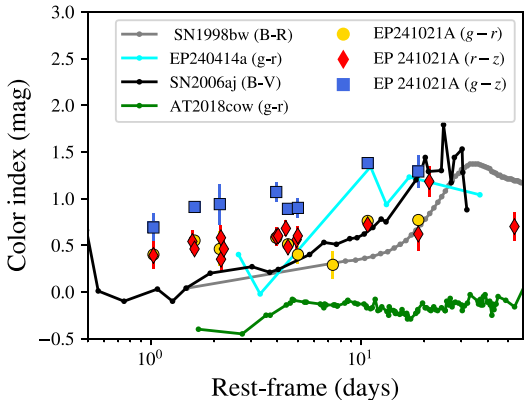

Figure A1. Colour evolution of EP241021a, compared to that of the transients AT 2018cow, SN 1998bw, SN 2006aj, and EP240414a (A. M. Soderberg et al. 2006; A. Clocchiatti et al. 2011; S. J. Prentice et al. 2018; J. N. D. Dalen et al. 2025). The squares, diamonds, and circles markers depict the respective $g-z$, $r-z$, and $g-r$ colours of EP241021a.

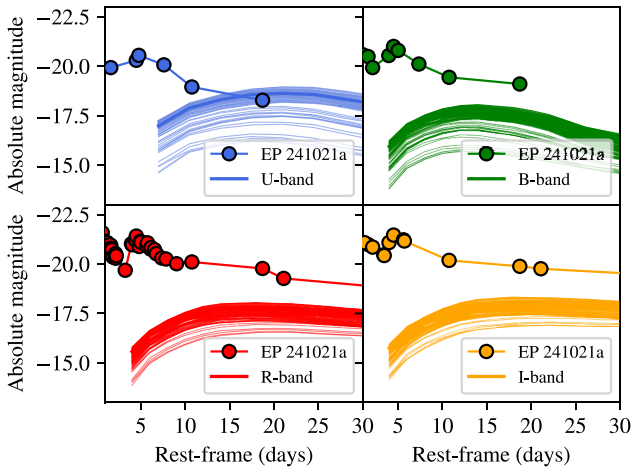

Figure A2. Optical light curves of EP241021a compared to optical thermonuclear transients from hydrodynamic simulation (considering a width range of orientations) of TDEs of WDs from M. MacLeod et al. (2016). The optical light curves remain brighter than the simulations during the whole emission.

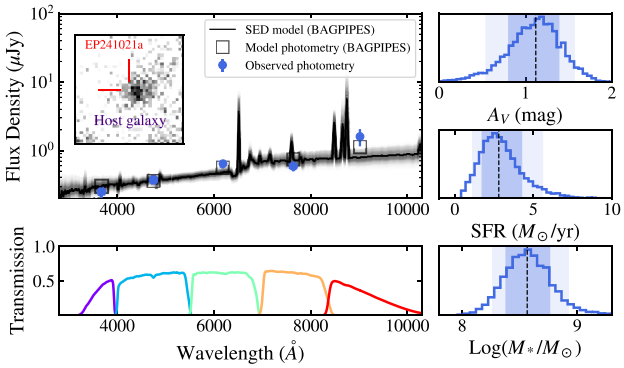

Figure A3. Main panel: posterior SED models for the host galaxy (observed by HiPERCAM using $ugriz$ bands) of EP241021a obtained from BAGPIPES. Bottom panel: the relative transmission functions of the different filters are used in the fitting process. Right panels: from top to bottom: the posterior distribution of the dust attenuation, the SFR, and the stellar mass. The colour gradient depicts the 68 per cent and 90 per cent confidence levels, respectively. The inset figure in the top main panel shows the image in r band taken by HiPERCAM $\sim$ 304 d after the trigger of the host galaxy of the transient. The lines mark the position of EP241021a.

Table A1. Photometry obtained with various ground-based telescopes for this work. UL in the AB magnitude column stands for the 3σ upper limit.

Telescope (1)	Instrument (2)	Date (UT) (3)	Days since trigger (4)	Exposure time (5)	Filter (6)	AB magnitude (7)	Ref. (8)
NOT	ALFOSC	2024-10-22 23:41:02	1.773	5×200	z	21.61±0.11	This work
NOT	ALFOSC	2024-10-23 03:01:58	1.91252	5×300	r	21.95±0.06	This work
NOT	ALFOSC	2024-10-23 23:19:27	2.75801	5×360	r	21.99±0.05	This work
NOT	ALFOSC	2024-10-24 00:48:23	2.81976	5×300	z	21.55±0.11	This work
GTC	HiPERCAM	2024-10-24 00:43:21	2.8232	40×30	u	22.85±0.04	This work
GTC	HiPERCAM	2024-10-24 00:43:21	2.8232	40×30	g	22.29±0.02	This work
GTC	HiPERCAM	2024-10-24 00:43:21	2.8232	40×30	r	21.84±0.02	This work
GTC	HiPERCAM	2024-10-24 00:43:21	2.8232	40×30	i	21.80±0.02	This work
GTC	HiPERCAM	2024-10-24 00:43:21	2.8232	40×30	z	21.48±0.03	This work
Swift	UVOT	2024-10-24 20:53:07	3.7236	2545.8	V	>20.69	This work
NOT	ALFOSC	2024-10-24 23:41:21	3.77322	5×300	r	22.26±0.05	This work
NOT	ALFOSC	2024-10-25 00:06:08	3.79042	5×300	z	22.01±0.12	This work
GS	GMOS-acq	2024-10-25 2:32:22	3.89231	1×60	r	22.37±0.08	This work
Keck	MOSFIRE	2024-10-25 9:57:55	4.201377	5×60	J	21.86±0.05	This work
Keck	MOSFIRE	2024-10-25 10:06:50	4.207569	6×30	H	21.76±0.12	This work
Keck	MOSFIRE	2024-10-25 10:19:38	4.216458	9×60	K_s	21.45±0.06	This work
Swift	UVOT	2024-10-25 15:30:30	4.47832	1347.82	$UVM2$	>22.49	This work
SOAR	Goodman	2024-10-27 03:08:35	5.917132	15×100	i	22.32±0.11	This work
GS	GMOS	2024-10-28 02:39:48	6.89714	4×180	r	21.76±0.01	This work
GS	GMOS	2024-10-28 02:52:48	6.91	4×180	g	22.24±0.02	This work
GS	GMOS-acq	2024-10-28 3:26:12	6.929699	1×60	z	21.27±0.10	This work
GS	GMOS-acq	2024-10-28 3:51:46	6.94745	1×60	i	21.7±0.05	This work
GTC	HiPERCAM	2024-10-29 01:31:00.9	7.8563	40×30	u	22.48±0.02	This work
GTC	HiPERCAM	2024-10-29 01:31:00.9	7.8563	40×30	g	21.78±0.01	This work
GTC	HiPERCAM	2024-10-29 01:31:00.9	7.8563	40×30	r	21.37±0.01	This work
GTC	HiPERCAM	2024-10-29 01:31:00.9	7.8563	40×30	i	21.32±0.01	This work
GTC	HiPERCAM	2024-10-29 01:31:00.9	7.8563	40×30	z	20.99±0.02	This work
Swift	UVOT	2024-10-29 09:32:49	8.3458	4289.06	U	22.23±0.24	This work
NOT	ALFOSC	2024-10-29 23:03:22	8.74684	3×300	r	21.68±0.06	This work
NOT	ALFOSC	2024-10-29 23:19:58	8.75836	3×300	g	21.98±0.07	This work
NOT	ALFOSC	2024-10-29 23:42:02	8.77369	5×300	z	21.18±0.08	This work
GTC	OSIRIS-acq	2024-10-31 00:36:59	9.81185	1×150	i	21.56±0.05	This work
SOAR	Goodman	2024-10-31 02:38:58	9.89648	20×60	r	21.87±0.08	This work
SOAR	Goodman	2024-10-31 04:30:17	9.9739	20×60	i	21.62±0.09	This work
GS	GMOS-acq	2024-10-31 6:16:25	10.04859	1×180	r	21.71±0.02	This work
NOT	ALFOSC	2024-10-31 23:18:48	10.75756	4×300	r	22.04±0.05	This work
NOT	ALFOSC	2024-11-1 23:55:37	11.78311	4×300	r	22.26±0.26	This work
SOAR	Goodman	2024-11-3 01:18:53	12.8409	25×60	g	22.67±0.11	This work
SOAR	Goodman	2024-11-3 01:56:03	12.86676	25×60	r	22.48±0.10	This work
Swift	UVOT	2024-11-03 02:25:38	13.2881	3059.02	U	22.71±0.43	This work
Swift	UVOT	2024-11-05 20:19:57	15.6522	985.45	U	>21.87	This work
NOT	ALFOSC	2024-11-5 23:57:39	15.78453	4×300	r	22.77±0.06	This work
Swift	UVOT	2024-11-07 02:11:57	17.1315	3107.47	U	>22.52	This work
GTC	HiPERCAM	2024-11-09 00:13:48	18.8027	40×30	u	23.83±0.09	This work
GTC	HiPERCAM	2024-11-09 00:13:48	18.8027	40×30	g	23.34±0.03	This work
GTC	HiPERCAM	2024-11-09 00:13:48	18.8027	40×30	r	22.68±0.04	This work
GTC	HiPERCAM	2024-11-09 00:13:48	18.8027	40×30	i	22.60±0.06	This work
GTC	HiPERCAM	2024-11-09 00:13:48	18.8027	40×30	z	22.06±0.05	This work
GTC	EMIR	2024-11-10 23:35:08	20.7688	260×5	H	22.39±0.09	This work
Swift	UVOT	2024-11-15 19:08:48	25.8468	1676.24	U	>22.22	This work
SOAR	Goodman	2024-11-18 03:12:09	27.92751	15×80	z	22.48±0.32	This work
SOAR	Goodman	2024-11-18 04:38:14	27.98729	15×80	r	>22.65	This work
GTC	HiPERCAM	2024-11-22 22:37:41	32.7359	40×30	u	24.50±0.12	This work
GTC	HiPERCAM	2024-11-22 22:37:41	32.7359	40×30	g	23.68±0.04	This work
GTC	HiPERCAM	2024-11-22 22:37:41	32.7359	40×30	r	23.01±0.05	This work
GTC	HiPERCAM	2024-11-22 22:37:41	32.7359	40×30	i	22.90±0.07	This work
GTC	HiPERCAM	2024-11-22 22:37:41	32.7359	40×30	z	22.49±0.17	This work
VLT	MUSE	2024-11-27 01:52:05	36.8956	3×700	r	23.51±0.11	This work
VLT	MUSE	2024-11-27 01:52:05	36.8956	3×700	i	23.02±0.11	This work
VLT	MUSE	2024-11-27 01:52:05	36.8956	3×700	z	22.43±0.12	This work
GS	GMOS	2024-12-29 01:23:20	68.86419	10×180	r	24.24±0.05	This work
GS	GMOS	2025-01-22 01:35:50	92.8616	12×80	z	23.94±0.22	This work
GS	GMOS	2025-01-23 00:57:01	93.83952	12×180	r	24.52±0.06	This work
GTC	HiPERCAM	2025-02-01 20:53:20.68	103.663	40×30	g	>24.69	This work
GTC	HiPERCAM	2025-02-01 20:53:20.68	103.663	40×30	r	>24.15	This work
GTC	HiPERCAM	2025-02-01 20:53:20.68	103.663	40×30	i	23.95±0.39	This work
GTC	HiPERCAM	2025-02-01 20:53:20.68	103.663	40×30	z	>24.18	This work

Notes. Columns 1 and 2: telescope and instrument per observation, respectively. Columns 3 and 4: start date of the observation and days after the X-ray trigger, respectively. Columns 5 and 6: exposure time and filter per observation, respectively. Column 7: magnitude and uncertainty in AB system. The photometry was not corrected for Galactic extinction, nor for the host contribution.

Table A2. Similar to Table A1, but considering only the photometry that is publicly available for EP241021a obtained with various ground-based telescopes.

Telescope (1)	Instrument (2)	Date (UT) (3)	Days since trigger (4)	Exposure time (5)	Filter (6)	AB magnitude (7)	Ref. (8)
KAIT	–	24-10-22 08:24:00	1.14	R	70×60	21.2±0.2	W. Zheng et al. (2024a)
DFOT	–	2024-10-22 16:48:07	1.49	R	12×300	21.62±0.1	A. K. Ror et al. (2024)
Liverpool Telescope	–	24-10-23 00:00:00	1.8	g	–	22.2±0.1	W. X. Li et al. (2024b)
Liverpool Telescope	–	24-10-23 00:00:00	1.8	r	–	21.9±0.1	W. X. Li et al. (2024b)
1m Las Cumbres observatory	–	24-10-23 07:12:00	2.1	i	–	21.7±0.1	W. X. Li et al. (2024a)
1m Las Cumbres observatory	–	24-10-23 07:12:00	2.1	r	–	21.9±0.1	W. X. Li et al. (2024a)
KAIT	–	24-10-23 07:55:12	2.12	R	70×60	21.7±0.3	W. Zheng et al. (2024a)
2.16m Xinglong	–	2024-10-23 15:57:29	2.42	V	3×600	22.5±0.5	J. J-Jin et al. (2024)
1-m SAO RAS	CCD-photometer	2024-10-23 19:27:12	2.61	R	9×300	21.81±0.06	A. S. Moskvitin, O. I. Spiridonova & GRB follow-up Team (2024a)
VLT	FORS2-acq	24-10-24 05:29:45	2.998	r	–	22.06±0.05	G. Pugliese et al. (2024)
Liverpool Telescope	–	2024-10-24 23:07:43	3.25	r	6×150	22.43±0.14	A. Bochenek & D. A. Perley (2024a)
Liverpool Telescope	–	2024-10-24 22:28:08.2	3.72	g	3×300	22.85±0.18	A. Kumar et al. (2024)
Liverpool Telescope	–	2024-10-24 22:44:16.8	3.73	i	3×300	21.93±0.15	A. Kumar et al. (2024)
Fraunhofer Telescope	3KK	2024-10-24 02:12:17	3.77	r	40×180	22.49±0.05	M. Busmann et al. (2024)
1-m SAO RAS	CCD-photometer	2024-10-26 20:39:47	5.65	R	12×300	23.10±0.18	A. S. Moskvitin, O. I. Spiridonova & GRB follow-up Team (2024b)
SOAR	Goodman	2024-10-27 04:56:18	6.004	i	4×300	22.36±0.07	J. Freeburn et al. (2024)
Fraunhofer Telescope	3KK	2024-10-28 21:08:46	7.67	J	5092	20.79 ± 0.10	M. Busmann et al. (2025)
1-m SAO RAS	CCD-photometer	2024-10-28 19:41:42	7.68	R	15×300	21.57±0.08	A. S. Moskvitin, O. I. Spiridonova & GRB follow-up Team (2024c)
Mephisto	–	2024-10-29 15:15:40	8.42	r	15×300	21.9±0.2	Y. Pan et al. (2024)
1-m SAO RAS	CCD-photometer	2024-10-29 19:55:32	8.64	R	12×300	21.64±0.05	A. S. Moskvitin et al. (2024c)
T193cm telescope	MISTRAL	2024-10-31 21:11:05	10.7	r	1×300s + 5×600	22.01±0.05	B. Schneider & C. Adami (2024)
Liverpool Telescope	–	2024-10-31 23:32:50	10.77	r	6×200	21.95±0.08	A. Bochenek & D. A. Perley (2024b)
1m LOT	–	2024-11-01 15:44:21	11.44	r	6×300	22.06±0.33	GCN 38042
T193cm telescope	MISTRAL	2024-11-03 20:29:00	13.7	r	12×600s	22.53±0.12	GCN 38071
Fraunhofer Telescope	3KK	2024-11-07 21:53:27	17.70	J	6790	21.93±0.16	M. Busmann et al. (2025)
GTC	EMIR	–	23.3	J	350	21.58±0.37	G. Gianfagna et al. (2025)
GTC	EMIR	–	23.3	H	462	21.98±0.39	G. Gianfagna et al. (2025)
GTC	EMIR	–	23.3	K_s	588	21.73±0.36	G. Gianfagna et al. (2025)
Fraunhofer Telescope	3KK	2024-11-16 18:12:12	26.54	r	4140	23.3±0.4	M. Busmann et al. (2025)
Fraunhofer Telescope	3KK	2024-11-16 18:12:12	26.54	z	3960	22.7±0.4	M. Busmann et al. (2025)
Fraunhofer Telescope	3KK	2024-11-24 20:59:37	34.66	J	8703	>21.7	M. Busmann et al. (2025)
Fraunhofer Telescope	3KK	2024-11-27 19:32:13	37.60	J	3565	>21.9	M. Busmann et al. (2025)

Table A3. X-ray detections of EP241021a used in this work.

Telescope (1)	Instrument (2)	Date (UT) (3)	Days since trigger (4)	Exp. time (ks) (5)	Band (keV) (6)	Γ (7)	Flux (erg s^{-1} cm^{-2}) (8)	Reference (9)
Einstein Probe	WXT	2024-10-21 05:07:56	Trigger	–	0.5–4.0	$1.48^{+1.24}_{-1.22}$	$\left(3.3^{+4.8}_{-1.6}\right) \times 10^{-10}$	J. W. Hu et al. (2024)
Swift	XRT	2024-10-24 20:58:09	3.7243	2.58	0.3–10	2.3 (fixed)	$< 2.5 \times 10^{-13}$	This work
Swift	XRT	2024-10-25 15:30:26	4.47828	1.38	0.3–10	2.3 (fixed)	$< 3.7 \times 10^{-13}$	This work
Swift	XRT	2024-10-29 09:32:45	8.34581	4.37	0.3–10	2.3 (fixed)	$\left(1.2^{+0.5}_{-0.4}\right) \times 10^{-13}$	This work
Swift	XRT	2024-11-03 02:25:34	13.288	3.11	0.3–10	2.3 (fixed)	$< 1.7 \times 10^{-13}$	This work
Chandra	ACIS-S	2024-11-04 02:51:52	13.97409	10.0	0.3–10	1.33 ± 0.65	$\left(6.5^{+3.1}_{-2.0}\right) \times 10^{-14}$	This work
						2.0 (fixed)	$\left(6.93^{+1.52}_{-1.32}\right) \times 10^{-14}$	This work
Swift	XRT	2024-11-05 20:24:10	15.64207	1.0	0.3–10	2.3 (fixed)	$< 4.9 \times 10^{-13}$	This work
Swift	XRT	2024-11-07 02:15:13	17.11778	3.2	0.3–10	2.3 (fixed)	$< 1.8 \times 10^{-13}$	This work
Swift	XRT	2024-11-15 19:08:44	25.84677	1.7	0.3–10	2.3 (fixed)	$\left(7.2^{+5.5}_{-3.7}\right) \times 10^{-14}$	This work
XMM–Newton	MOS2	2025-01-18 13:03:43	89.34	39.9	0.3–10	–	$< 2.83 \times 10^{-15}$	X. Shu et al. (2025)
				Einstein Probe satellite				
Einstein Probe	FXT	2024-10-22 17:43:00	1.54	3.0	0.3–10	1.83±0.08	$\left(2.10^{+0.32}_{-0.28}\right) \times 10^{-13}$	X. Shu et al. (2025)
Einstein Probe	FXT	2024-10-23 17:46:00	2.54	6.0	0.3–10	–	$\left(2.0^{+0.19}_{-0.18}\right) \times 10^{-13}$	X. Shu et al. (2025)
Einstein Probe	FXT	2024-10-24 19:25:00	3.61	6.0	0.3–10	–	$\left(1.45^{+0.18}_{-0.16}\right) \times 10^{-13}$	X. Shu et al. (2025)
Einstein Probe	FXT	2024-10-25 17:51:00	4.54	8.6	0.3–10	–	$\left(1.41^{+0.14}_{-0.15}\right) \times 10^{-13}$	X. Shu et al. (2025)
Einstein Probe	FXT	2024-10-27 14:47:00	6.41	6.1	0.3–10	–	$\left(1.66^{+0.20}_{-0.18}\right) \times 10^{-13}$	X. Shu et al. (2025)
Einstein Probe	FXT	2024-10-29 08:28:00	8.15	5.6	0.3–10	–	$\left(2.09^{+0.25}_{-0.18}\right) \times 10^{-13}$	X. Shu et al. (2025)
Einstein Probe	FXT	2024-11-02 15:04:00	12.43	2.1	0.3–10	–	$\left(0.91^{+0.26}_{-0.22}\right) \times 10^{-13}$	X. Shu et al. (2025)
Einstein Probe	FXT	2024-11-04 07:08:00	14.10	6.2	0.3–10	–	$\left(0.79^{+0.14}_{-0.13}\right) \times 10^{-13}$	X. Shu et al. (2025)
Einstein Probe	FXT	2024-11-07 12:04:00	17.30	4.8	0.3–10	–	$\left(0.87^{+0.18}_{-0.15}\right) \times 10^{-13}$	X. Shu et al. (2025)
Einstein Probe	FXT	2024-11-20 15:41:00	30.45	5.6	0.3–10	–	$\left(0.47^{+0.13}_{-0.11}\right) \times 10^{-13}$	X. Shu et al. (2025)
Einstein Probe	FXT	2024-11-30 19:13:00	40.60	8.9	0.3–10	–	$\left(0.31^{+0.10}_{-0.09}\right) \times 10^{-13}$	X. Shu et al. (2025)
Einstein Probe	FXT	2025-01-08 10:36:19	79.24	8.7	0.3–10	–	$< 1.82 \times 10^{-14}$	X. Shu et al. (2025)

Notes. Columns 1 and 2: telescope and instrument per observation, respectively. Columns 3 and 4: start date of the observation and days after the X-ray trigger, respectively. Columns 5 and 6: exposure time and energy band per observation, respectively. Column 7: photon index computed or assumed. Column 8: unabsorbed flux. Column 9: reference.

Table A4. Radio observations of EP241021a used in this work.

Telescope (1)	Start date (UT) (2)	Since trigger (d) (3)	Frequency (GHz) (4)	Flux density (mJy) (5)	Reference (6)
ATCA	2024-10-29	8.0	5.0	0.350±0.029	X. Shu et al. (2025)
ATCA	2024-10-29	8.0	5.5	0.382±0.024	X. Shu et al. (2025)
ATCA	2024-10-29	8.0	6.0	0.407±0.029	X. Shu et al. (2025)
ATCA	2024-10-29	8.0	9.0	0.453±0.026	X. Shu et al. (2025)
ATCA	2024-10-29	8.0	9.5	0.467±0.028	X. Shu et al. (2025)
ATCA	2024-11-08 8:52:55	18.3	5.5	0.434±0.022	M. Yadav et al. (2025)
ATCA	2024-11-08 8:52:55	18.3	9.0	0.543±0.024	M. Yadav et al. (2025)
ATCA	2024-11-08 8:52:55	18.3	17.0	0.366±0.035	M. Yadav et al. (2025)
ATCA	2024-11-11	21.1	2.1	0.256±0.042	G. Gianfagna et al. (2025)
e-MERLIN	2024-11-09	19.5	5.0	0.614±0.164	G. Gianfagna et al. (2025)
ATCA	2024-11-15	25.1	5.5	0.842±0.044	G. Gianfagna et al. (2025)
ATCA	2024-11-15	25.1	9.0	0.653±0.034	G. Gianfagna et al. (2025)
ATCA	2024-11-15	25.1	16.7	0.341±0.029	G. Gianfagna et al. (2025)
ATCA	2024-11-15 7:36:25	25.3	17.0	0.347±0.041	M. Yadav et al. (2025)
ATCA	2024-11-15	25.1	21.0	0.285±0.092	G. Gianfagna et al. (2025)
ATCA	2024-11-21	31.6	2.1	0.327±0.033	G. Gianfagna et al. (2025)
ATCA	2024-11-21	31.6	5.5	1.07±0.09	G. Gianfagna et al. (2025)
ATCA	2024-11-21	31.6	9.0	1.1±0.07	G. Gianfagna et al. (2025)
VLBA	2024-11-28	37.0	6.2	0.774±0.072	X. Shu et al. (2025)
VLBA	2024-11-40	39.0	8.4	0.762±0.081	X. Shu et al. (2025)
ATCA	2024-11-24 7:01:00	34.1	17.0	0.450±0.046	M. Yadav et al. (2025)
ATCA	2024-11-24	34.1	16.7	0.393±0.061	G. Gianfagna et al. (2025)

Notes. Column 1: telescope per observation. Columns 2 and 3: start day of the observation and the day since the X-ray trigger, respectively. Columns 4, 5, and 6: frequency, flux density per observation (mJy units), and references, respectively.

Table A5. Spectroscopy obtained with various ground-based telescopes for this work.

Telescope (1)	Instrument (2)	Start date (UT) (3)	Since trigger (d) (4)	Exp. time (s) (5)	Grism/grating (6)
VLT	FORS2	2024-10-24 05:19:51	3.02246	2×1200	GRIS_300V
GS	GMOS	2024-10-25 02:40:34	3.9254	4×900	*R*400
GS	GMOS	2024-10-28 04:03:47	6.992	4×1500	*R*400
GTC	OSIRIS +	2024-10-31 00:45:06	9.8505	3×1800	*R*500*R*
GS	GMOS	2024-10-31 06:27:26	10.085	4×1200	*R*400
GTC	OSIRIS +	2024-11-09 23:16:22	19.7874	3×1800	*R*300*B*
VLT	MUSE	2024-11-27 01:52:05	36.8956	4×700	–

Table A6. Redshifts obtained from fitting the brightest emission lines per spectrum.

Epoch (1)	Lines (2)	z (3)
GMOS 1	3727, H_β, 4959, 5007 Å	0.7486 per cent±0.0001
GMOS 2	3727, H_β, 4959, 5007 Å	0.7486 per cent±0.0006
GMOS 3	H_β, 5007 Å	0.7487 per cent±0.0001
OSIRIS 1	3727, 4959, 5007 Å	0.7488 per cent±0.0001
OSIRIS 2	3727, 4959, 5007 Å	0.7481 per cent±0.0002
MUSE	H_β, 4959, 5007 Å	0.7484 per cent±0.0001

Notes. Columns 1 and 2: spectroscopic epoch and emission lines used for measuring redshifts. Column 3: redshift obtained for each spectroscopic epoch. The mean redshift value from fitting emission lines is $\overline{z} = 0.7485$.

Table A7. Posteriors of the models obtained fitting the SED of the transient at different epochs (see Section 4.3). The parameters are at 99 per cent confidence level.

Epoch (d) (1)	$\log(\nu_m/\mathrm{Hz})$ (2)	$\log(\nu_c/\mathrm{Hz})$ (3)	$F_{\max}$ (mJy) (4)	p (5)	$T_{\rm BB}$ ($\times 10^3$ K) (6)	$R_{\rm BB}$ ($\times 10^{15}$ cm) (7)	BIC (8)
2.8	$12.34^{+0.16}_{-0.37}$	$18.21^{+0.79}_{-1.49}$	$2.18^{+0.97}_{-1.12}$	$2.96^{+0.20}_{-0.18}$	–	–	−70.59
8.3	$12.5^{+0.0}_{-0.03}$	$18.14^{+0.86}_{-1.26}$	2.6 ± 0.17	3.01 ± 0.03	–	–	294.85
18.2	$10.22^{+0.11}_{-0.09}$	$17.94^{+1.05}_{-1.76}$	0.54 ± 0.05	$2.33^{+0.12}_{-0.16}$	$8.93^{+0.68}_{-0.82}$	$5.29^{+0.92}_{-0.85}$	−284.82
24.5	$9.75^{+0.27}_{-0.25}$	$18.0^{+0.99}_{-1.97}$	$1.14^{+0.62}_{-0.38}$	$2.3^{+0.13}_{-0.22}$	$5.6^{+4.32}_{-1.60}$	$10.81^{+15.6}_{-10.79}$	−312.29
31.8	$10.32^{+0.18}_{-0.14}$	$18.09^{+0.91}_{-2.06}$	$1.01^{+0.20}_{-0.15}$	$2.5^{+0.49}_{-0.21}$	$8.52^{+1.26}_{-1.37}$	$4.56^{+1.92}_{-4.35}$	−193.44
37.5	$9.93^{+0.32}_{-0.43}$	$17.14^{+0.86}_{-0.63}$	$0.99^{+1.18}_{-0.31}$	$2.38^{+0.25}_{-0.14}$	$5.28^{+3.86}_{-1.85}$	$12.81^{+38.82}_{-9.86}$	−201.03

This paper has been typeset from a TEX/LATEX file prepared by the author.